

THE COOPERATIVE JAHN-TELLER TRANSITION
IN SOME RARE EARTH ARSENATES

A STUDY OF THE COOPERATIVE JAHN-TELLER
TRANSITION IN SOME RARE EARTH ARSENATES
BY X-RAY DIFFRACTION

by

FREDERICK G. LONG, B.A.

A Thesis

Submitted to the School of Graduate Studies

in Partial Fulfilment of the Requirements

for the Degree

Doctor of Philosophy

McMaster University

January 1977

DOCTOR OF PHILOSOPHY (1977)
(Physics)

McMASTER UNIVERSITY
Hamilton, Ontario

TITLE: A study of the cooperative Jahn-Teller transition
in some rare earth arsenates using X-ray diffraction

AUTHOR: Frederick George Long, B.A. (Essex University)

SUPERVISOR: Professor C. V. Stager

NUMBER OF PAGES: xi,113

SCOPE AND CONTENTS:

A low temperature single crystal X-ray diffractometer has been designed and constructed. This has been used to determine the crystal structure of dysprosium arsenate and terbium arsenate at 6°K. These structures are compared with those found at room temperature. This comparison is used to gain information about the ionic coupling mechanism which drives a cooperative Jahn-Teller transition in these compounds at temperatures below 30°K. Further information about these transitions is obtained from a study of the temperature dependence of the lattice strain.

ABSTRACT

A low temperature single crystal X-ray diffractometer has been designed and constructed. This has been used to determine the crystal structure of dysprosium arsenate and terbium arsenate at 6°K. These structures are compared with those found at room temperature. This comparison is used to gain information about the ionic coupling mechanism which drives a cooperative Jahn-Teller transition in these compounds at temperatures below 30°K. Further information is obtained from a study of the temperature dependence of the lattice strain, which is proportional to the order parameter for the transition. For TbAsO_4 it is found that the coupling is long range, and that the dominant mechanism is via the lattice strain. The ionic interaction in DyAsO_4 is found to be short range; coupling to both lattice strain and phonons are important in this case.



ACKNOWLEDGEMENTS

I would like to thank my supervisor, Dr. C. V. Stager, for his patience and his continued assistance with this work.

I am also indebted to Dr. C. Calvo, for help with the crystallographic aspect of this work, to Dr. M. F. Collins for many helpful discussions, to S. Kocsis and the instrument machine shop staff for constructing much of the apparatus used, to J. Neimanis for assistance with the experimental work, and to Mrs. H. Kennelly for typing the manuscript.

Finally I wish to thank my wife Debbie, to whom I dedicate this work, for her patience and support.

TABLE OF CONTENTS

<u>CHAPTER</u>		<u>PAGE</u>
1	INTRODUCTION	1
	Sample preparation	4
2	X-RAY SCATTERING BY CRYSTALS	6
	The crystal lattice	6
	X-ray scattering by atoms	7
	X-ray scattering by a crystal	8
	The Ewald sphere	10
	The structure factor	12
	Polarization correction	14
	Lorentz effect	14
	Absorption correction	14
	Secondary extinction	15
	Thermal motion	16
3	REFINEMENT OF THE CRYSTAL STRUCTURE OF THE ARSENATES AND VANADATES OF TERBIUM AND DYSPROSIUM AT 300°K	18
	Introduction	18
	Refinement of structures	19
	Discussion	21
	The Crystal field at the rare earth site	24
4	THE LOW TEMPERATURE DIFFRACTOMETER	41
	The Cryostat	41
	Sample holder	44
	Mounting table	46

<u>CHAPTER</u>		<u>PAGE</u>
	Detector and camera	49
	Alignment of the diffractometer	52
	Alignment of sample	52
5	REFINEMENT OF THE LOW TEMPERATURE CRYSTAL STRUCTURES OF DyAsO ₄ and TbAsO ₄	57
	Introduction	57
	Domains	59
	Refinement	61
	Discussion	64
	DyAsO ₄	65
	TbAsO ₄	66
6	THEORY OF THE PHASE TRANSITION IN THE RARE EARTH VANADATES AND ARSENATES	77
	Introduction	77
	The Jahn-Teller theorem	78
	Electron states	79
	Single ion-lattice coupling	81
	Crystal field	83
	Electron-phonon coupling	83
	Molecular field theory	85
	Strain coupling	87
7	THE JAHN-TELLER TRANSITION IN DyAsO ₄ AND TbAsO ₄	93
	Measurement of the order parameter	93
	Temperature dependence of the order para- meter for DyAsO ₄	94
	Temperature dependence of the order para- meter for TbAsO ₄	99
	Optical phonon coupling	102

<u>CHAPTER</u>		<u>PAGE</u>
8	THE COOPERATIVE JAHN-TELLER EFFECT IN THE MIXED CRYSTALS $Tb_xR_{1-x}AsO_4$ (R = Gd, Y or La)	103
9	CONCLUSIONS	108
	BIBLIOGRAPHY	111

LIST OF FIGURES

<u>FIGURE NO.</u>		<u>PAGE</u>
2.1	The Ewald construction	11
3.1	Schematic representation of the tetra- gonal zircon structure	22
3.2	Environment of the rare earth ion in the zircon structure	25
4.1	Sectional drawing of the cryostat used with the low temperature diffractometer	42
4.2	Sectional drawing of the sample holder used at low temperatures	45
4.3	Construction of the mounting table for the cryostat	47
4.4	The detector housing mounted on the horizontal goniometer	50
4.5	The low temperature diffractometer in use	51
4.6	Appearance of zero-layer lines on oscillation photographs of a misaligned crystal	53
5.1	A reciprocal lattice plane ($\ell = \text{constant}$) for a crystal consisting of two domains whose common boundary is a (110) plane	60
5.2	The mode of distortion of the AsO_4^{3-} tetrahedra in DyAsO_4	66
5.3	The mode of distortion of the AsO_4^{3-} tetrahedra in TbAsO_4	68
6.1	The lowest electronic states of Dy^{3+} and and Tb^{3+} ions above and below the Jahn- Teller transition temperatures	80
7.1	Temperature dependence of the order para- meter for DyAsO_4	95
7.2	Asymptotic behaviour of the order para- meter yielding the critical exponent β for DyAsO_4	98

<u>FIGURE NO.</u>		<u>PAGE</u>
7.3	Temperature dependence of the order parameter for TbAsO_4	100
7.4	Asymptotic behaviour of the order parameter yielding the critical exponent β for TbAsO_4	101
8.1	The variation of transition temperature with composition for the system $\text{Tb}_x\text{R}_{1-x}\text{AsO}_4$ (R = gd, Y or La)	106
8.2	Temperature dependence of the strain for the mixed crystals $\text{Tb}_x\text{R}_{1-x}\text{AsO}_4$ (R = gd, Y or La)	107

LIST OF TABLES

<u>TABLE NO.</u>		<u>PAGE</u>
3.1a	Crystal data for DyVO ₄ at 300°K	29
3.1b	Crystal data for DyAsO ₄ at 300°K	30
3.1c	Crystal data for TbVO ₄ at 300°K	31
3.1d	Crystal data for TbAsO ₄ at 300°K	32
3.2a	Atomic parameters for DyVO ₄	33
3.2b	Atomic parameters for DyAsO ₄	33
3.2c	Atomic parameters for TbVO ₄	34
3.2d	Atomic parameters for TbAsO ₄	34
3.3a	Bond lengths and angles for DyVO ₄	35
3.3b	Bond lengths and angles for DyAsO ₄	35
3.3c	Bond lengths and angles for TbVO ₄	36
3.3d	Bond lengths and angles for TbAsO ₄	36
3.4a	Observed and calculated structure factors for DyVO ₄	37
3.4b	Observed and calculated structure factors for DyAsO ₄	38
3.4c	Observed and calculated structure factors for TbVO ₄	39
3.4d	Observed and calculated structure factors for TbAsO ₄	40
5.1a	Crystal data for DyAsO ₄ at 6°K	70
5.1b	Crystal data for TbAsO ₄ at 6°K	71
5.2a	Atomic parameters for DyAsO ₄ at 6°K	72
5.2b	Atomic parameters for TbAsO ₄ at 6°K	72

TABLE NO.PAGE

5.3a	Bond lengths and angles for DyAsO ₄ at 6°K	73
5.3b	Bond lengths and angles for TbAsO ₄ at 6°K	74
5.4a	Observed and calculated structure factors for DyAsO ₄ at 6°K	75
5.4b	Observed and calculated structure factors for TbAsO ₄ at 6°K	76
6.1	Comparison of the observed and calculated transition temperatures for the rare earth arsenates and vanadates	91

CHAPTER 1

INTRODUCTION

Recently great progress has been made in the understanding of the cooperative Jahn-Teller effect. This is partly due to the discovery of the effect in a number of rare earth compounds with the zircon structure. In these compounds there is a phase transition which is driven by the interaction of the electronic states of certain of the ions with the lattice phonons. For the rare earth compounds this transition is of second order and involves a crystallographic phase change. The family of rare earth compounds in which the effect was recently discovered are the arsenates and vanadates of terbium, thulium and dysprosium. Prior to this discovery, most of the work on the cooperative Jahn-Teller effect involved spinels containing transition metal ions. The studies made on these compounds are reviewed by Engleman (1972). The spinels are not as suitable for extensive study for two major reasons; first the crystals are not transparent and second the cubic symmetry of the crystals introduces certain theoretical difficulties. The opaqueness of the crystals prevents a direct study of the electronic energy levels using optical techniques. The cubic symmetry requires that the ionic coupling be through degenerate phonon states.

In the case of the rare earth salts, their tetragonal symmetry allows coupling via non-degenerate lattice modes. This makes a theoretical treatment of the transition much more simple. Two further advantages of the rare earth compounds, that make them ideal for study, are their transparency and their low transition temperatures (3°K to 30°K). The latter property allows studies of the specific heat anomalies, associated with the transitions, to be made without interference from thermal phonon effects. A recent review by Gehring and Gehring, (1975) gives a summary of the work to date on these, and other, compounds that exhibit the cooperative Jahn-Teller effect.

The amount of work that has been done on the rare earth compounds is quite extensive, however, details of the atomic arrangements in the low temperature structures are not available. It is the primary purpose of this work to fill this gap. A single crystal low temperature X-ray diffractometer has been designed and constructed. This was used to determine the structures of DyAsO_4 and TbAsO_4 at 6°K . These structures are expected to be the same for the respective vanadates, due to the great similarity in physical properties between the arsenates and vanadates. The salts of thulium were not studied because their transition temperatures are much lower. Such a study would require a more expensive and more complicated cryogenic system.

The low temperature structure allows an estimate of quantities associated with the phase transition to be made. By comparing the high and low temperature structures the symmetry and magnitude of the coupling to the phonon modes responsible for the transition can be determined. A measurement of the temperature dependence of the lattice strain, which is the order parameter for the transitions, gives information about the range of the ionic coupling.

A theoretical treatment of these transitions has been given by Elliot et al. (1972) using a mean field approach. This is found to give a good description of the transition in the terbium and thulium compounds, but meets only limited success in the dysprosium case. The failure is due to the short range nature of the interaction between the dysprosium ions. To further test the theory as applied to $TbAsO_4$, a study was made of the order parameter in various mixed systems, where some of the terbium ions are replaced with non Jahn-Teller ions (Gd, V and La). All of the above measurements of strain were made using the low temperature diffractometer.

The remainder of Chapter 1 is devoted to a description of the method of sample preparation. Chapter 2 contains a review of the theory of X-ray diffraction by crystals. Chapter 3 describes the determination of the room temperature crystal structure of some rare earth arsenates and vanadates. A description of the low temperature diffractometer is given in Chapter 4, together with a procedure for its use. The

determination of the low temperature structure is given in Chapter 5. Chapter 6 contains an outline of the mean field theory developed by Elliot et al. (1972) to describe the Jahn-Teller transitions in the rare earth compounds. Chapter 7 contains the results of the strain measurements on TbAsO_4 and DyAsO_4 together with the analysis of the structural results in terms of the mean field theory. Chapter 8 describes the results obtained for the mixed terbium salts and Chapter 9 summarizes the main results of this work.

Sample Preparation

The flux method (Fiegelson, 1964) was used to grow the RXO_4 (R=rare earth, X=V,As) crystals.

A platinum crucible was almost completely filled with either lead pyrovanadate ($\text{Pb}_2\text{V}_2\text{O}_7$) or lead pyroarsenate ($\text{Pb}_2\text{As}_2\text{O}_7$). The rare earth oxide (Tb_2O_3 or Dy_2O_3) was added and the crucible tightly covered. The ratio of the lead compound to the oxide was 30:1 by weight.

The crucible was heated to 1300°C at a rate of $200^\circ\text{C}/\text{hour}$ and allowed to soak for 10 hours to assure complete dissolution of the oxide. It was then cooled to 900°C at a rate of $2^\circ\text{C}/\text{hour}$, then quenched to room temperature by turning off the furnace. The solidified flux ($\text{Pb}_2\text{V}_2\text{O}_7$ or $\text{Pb}_2\text{As}_2\text{O}_7$), in which the crystals were imbedded, was removed by leaching with hot dilute nitric acid.

The crystals grow as rods, almost square in cross-section. Investigation of the crystals by x-ray diffraction, using a precession camera, revealed that the rod axis was [001] and that the long faces were the (100) and (010) planes.

For the mixed crystals the terbium oxide was replaced by a suitable mixture of terbium oxide and either gadolinium oxide, yttrium oxide or lanthanum oxide. The composition of the mixed crystals was determined by electron microprobe analysis of a number of crystals of each composition.

CHAPTER 2

X-RAY SCATTERING BY CRYSTALS

In this chapter the theory of diffraction of X-rays by crystals will be reviewed. The material given here is only intended as an outline, more details may be found in the many texts on the subject (e.g. Stout and Jensen, 1968).

The Crystal Lattice

A crystal may be regarded as a three dimensional periodic array of lattice points, with the same arrangement of atoms around each point. A grid of lines may be used to connect the lattice points. This grid can be described by the direction and magnitude of three grid lines \underline{a} , \underline{b} and \underline{c} . These are three non-coplanar vectors which, by repeated action are sufficient to construct the lattice. There are many different choices for the unit vectors. Each choice defines a different parallelepiped, the unit cell. The unit cell with the minimum volume is termed primitive. The cell selected for actual use is usually primitive, however sometimes a larger cell with higher symmetry is chosen.

If there is an atom at a position \underline{r} relative to some origin, then there will be an equivalent atom at

$$\underline{r}' = \underline{r} + u\underline{a} + v\underline{b} + w\underline{c} , \quad (2.1)$$

where u , v and w are integers. Successive atoms generated using the above formula are in different unit cells, however other similar atoms in any given unit cell can be generated by applying the crystal symmetry elements. Combining the translations given by equation (2.1) with the symmetry operations will give all the atomic positions. The resulting atomic arrangement then conforms to the space group symmetry of the crystal. The importance of symmetry on the X-ray diffraction pattern will be evident later.

X-ray Scattering by Atoms

Atoms scatter X-rays because they are made up of charged particles. If such a particle happens to be in the path of an X-ray wave, it is set into forced oscillations by the changing electric field of the wave. This accelerating charge then emits radiation of the same wavelength as the original wave according to the Thomson formula. For an unpolarized incident wave the intensity is given by

$$I_e = I_0 \left(\frac{\mu_0}{4\pi}\right)^2 \frac{e^2}{m^2} \left(\frac{1+\cos 2\theta}{2}\right) \quad (2.2)$$

where 2θ is the angle between the incident and scattered waves. The final term arises because the scattering efficiency of the charge depends on the angle between the polarization of the incident beam and the direction of scattering. The $1/m^2$ dependence shows that the nuclear scattering may be ignored. Each electron in an atom will scatter X-rays according to equation (2.2), however, because the spatial separation of the electrons

is of the same magnitude as the wavelength (λ) of the radiation, the individual waves will interfere. This has the effect of reducing the radiation scattered by an atom below ZI_e , where Z is the atomic number. Instead the scattered intensity will be given by

$$I_a = I_e f^2(2\theta). \quad (2.3)$$

$f(2\theta)$ is called the atomic scattering factor and is the ratio of the amplitude scattered by the atom to that scattered by an electron at the atomic centre. If the distribution of electrons around the nucleus is spherically symmetric and is given by $\rho(r)$, then

$$f(\underline{G}) = \int \rho(r) e^{-i\underline{G} \cdot \underline{r}} d\underline{r}. \quad (2.4)$$

\underline{G} is the scattering vector and is given by

$$\underline{G} = \underline{k} - \underline{k}_0; \quad (|\underline{G}| = \frac{2\sin\theta}{\lambda}), \quad (2.5)$$

where \underline{k} and \underline{k}_0 are vectors along the scattered and incident waves with magnitude $1/\lambda$. The distribution function $\rho(r)$ can be calculated from the electronic wavefunctions ψ_i .

$$\rho(r) = \sum_i \psi_i \psi_i^*. \quad (2.6)$$

X-ray Scattering by a Crystal.

Since the atomic separations in a crystal are of the same magnitude as λ , waves scattered by the individual atoms will interfere. If we consider an atom at the same site in

two different unit cells, then from (2.1) the vector joining the atoms can be written as

$$\underline{r} = u\underline{a} + v\underline{b} + w\underline{c} . \quad (2.7)$$

For the waves scattered from the two atoms to be in phase we require that

$$\underline{G} \cdot \underline{r} = 1, 2, 3 \text{ etc.} . \quad (2.8)$$

If the waves scattered by atoms at the same site in all unit cells are to be in phase, then equation (2.8) must hold for all values of u , v and w , i.e.

$$\underline{G} \cdot \underline{a} = h; \quad \underline{G} \cdot \underline{b} = k; \quad \underline{G} \cdot \underline{c} = l , \quad (2.9)$$

where h , k and l are integers. These conditions on \underline{G} require that

$$\underline{G} = h\underline{a}^* + k\underline{b}^* + l\underline{c}^* , \quad (2.10)$$

where

$$\underline{a}^* = \frac{\underline{b} \times \underline{c}}{V} ; \quad \underline{b}^* = \frac{\underline{a} \times \underline{c}}{V} ; \quad \underline{c}^* = \frac{\underline{a} \times \underline{b}}{V} . \quad \circ (2.11)$$

V is the volume of the unit cell. Thus the scattering vectors fall on the lattice points of a new lattice, the reciprocal lattice, defined by \underline{a}^* , \underline{b}^* and \underline{c}^* . To obtain any significant scattered intensity, atoms at the same site in all unit cells must scatter in phase, so the scattered intensity is proportional to the square of the amplitude scattered by a single unit cell. The condition for significant scattering given by (2.10) can be regarded as reflections from families of lattice

planes, whose interplanar spacing is $1/|G|$. The lattice planes are characterized by their Miller indices, h , k and l . For this reason the diffraction peaks are commonly referred to as reflections.

The Ewald Sphere

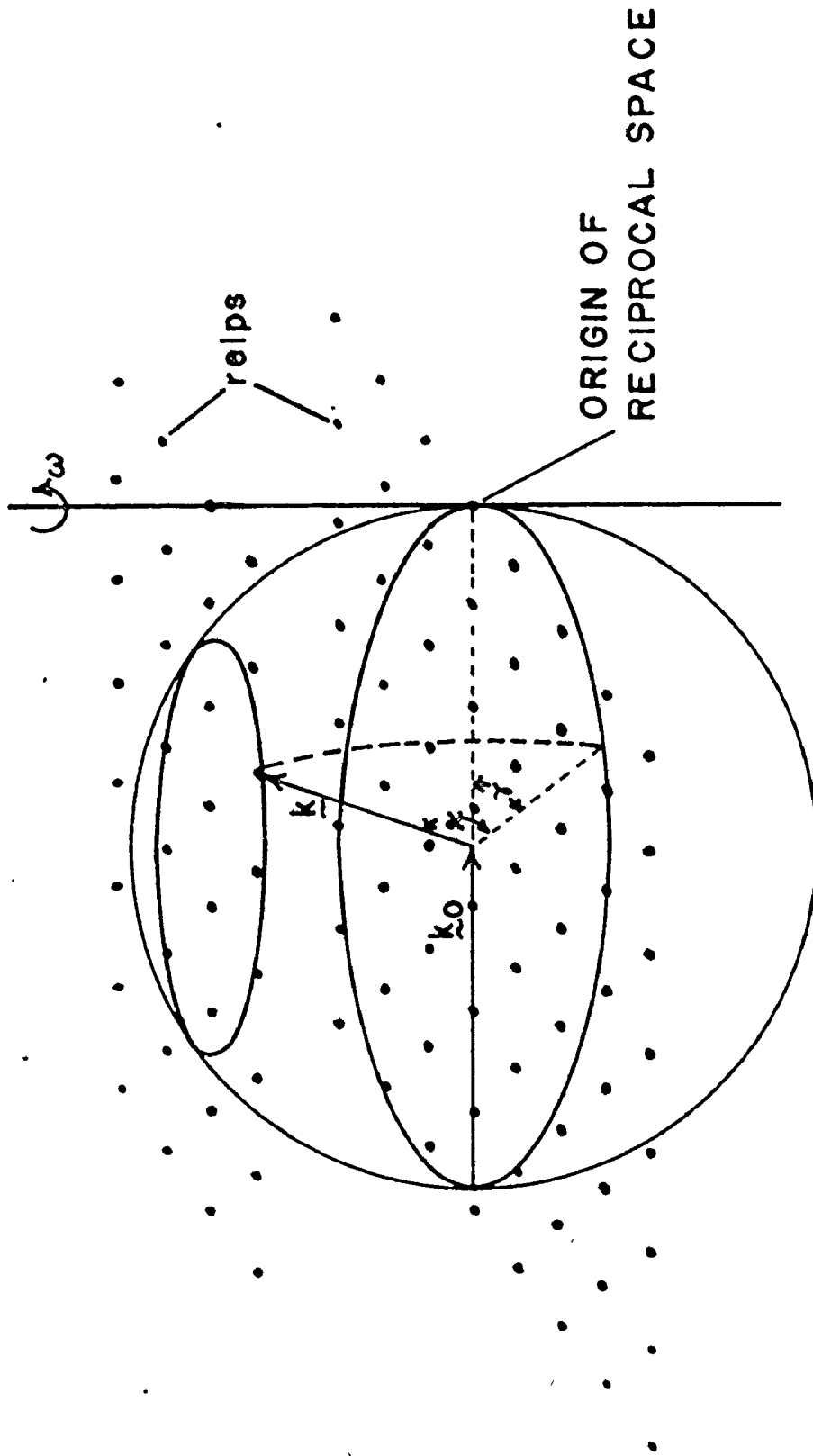
It is convenient, in describing diffraction in different experimental geometries, to use the Ewald construction. This is shown in Fig. 2.1. A sphere of radius $1/\lambda$ is constructed in the reciprocal space of the crystal, such that the origin of the space is on the surface of the sphere in its equatorial plane. The incident beam is defined by the vector k_0 . The reciprocal lattice can be manipulated, by moving the crystal, so that a given reciprocal lattice point (relp) lies on the sphere. The diffracted beam corresponding to this relp is then given by the vector k .

In the Eulerian cradle geometry of most modern diffractometers the crystal is manipulated so that the required relp is in the equatorial plane of the sphere. Then the crystal is rotated about the ω axis, which is normal to this plane, to bring the relp into a position for diffraction.

For the normal beam Weissenberg geometry the reciprocal lattice is fixed, apart from rotations about the ω axis. If a real lattice vector is parallel to this axis the relps will fall on planes parallel to the equatorial plane. The diffracted beam is then restricted to a few circles (layer lines) on the

Fig. 2.1

The Ewald Construction



sphere. The angle between \underline{k} and the w axis is defined to be $(\pi/2 - \chi)$, and the angle between \underline{k}_0 and the projection of \underline{k} onto the equatorial plane to be γ . These angles are shown in Fig. 2.1.

The Structure Factor

If there is more than one atom in a unit cell the waves scattered by each atom will have a different phase. Hence the total amplitude scattered by a unit cell will be reduced from the sum of the individual scattering factors. The position of the j th atom in the unit cell can be written as

$$\underline{r}_j = u_j \underline{a} + v_j \underline{b} + w_j \underline{c} . \quad (2.12)$$

If we consider the phase of waves scattered from the origin to be zero, then the total amplitude scattered by a unit cell is

$$\begin{aligned} F(\underline{G}) &\propto \sum_j f_j(\underline{G}) e^{-i \underline{G} \cdot \underline{r}_j} \\ &= \sum_j f_j(\underline{G}) e^{-i (h u_j + k v_j + l w_j)} . \end{aligned} \quad (2.13)$$

$F(\underline{G})$ is known as the structure factor and in general is a complex quantity. It can be shown quite generally that the Fourier transform of the structure factors equals the electron density in the unit cell. Hence, if these quantities can be measured, for an unknown structure, the atomic positions can be determined. If the unit cell chosen is non-primitive, some of the structure factors will be zero. There will be similar systematic

absences if the lattice contains translational symmetry elements, i.e. screw axes or glide planes. These missing reflections help to determine the space group of the crystal.

The intensity of radiation scattered by a crystal can be written

$$C(\underline{G}) I(\underline{G}) = K I_e |F(\underline{G})|^2 \quad (2.14)$$

where $C(\underline{G})$ represents various corrections that must be applied to the measured intensities $I(\underline{G})$ before comparison with the calculated intensities and K is a scale constant. Measuring these intensities permits the determination of the magnitude of the structure factors. However, the phase of these quantities cannot be measured. This is the so called phase problem in crystallography. The phase problem prevents a straightforward determination of atomic positions. There are many methods to overcome this problem, these may be found in texts on X-ray crystallography. For the structures considered in this work, the atomic positions were either known or were determined by other means, so further consideration of the phase problem will not be given here.

Once a suitable model for the structure has been decided upon, the model may be refined by the method of least squares. In this method the magnitude of the observed and calculated structure factors (F_c and F_o) are compared, and adjustments are made to the model to minimise

$$R = \frac{\sum_j (|F_o^j| - |F_c^j|)^2}{\sum |F_o^j|^2} \quad (2.15)$$

Before one can obtain the observed structure factors from the square roots of the measured intensities, the intensities must be corrected for certain geometrical and physical effects.

Polarization Correction

This effect has been considered in connection with the Thomson formula (2.2). To correct for this the measured intensity must be multiplied by p^{-1} , where

$$p = \frac{1 + \cos^2 2\theta}{2} \quad (2.16)$$

Lorentz Effect

This effect is dependent on the geometry of the instrument used for the intensity measurement. It arises because different relps take different times to pass through the Ewald sphere. To correct for this the intensity is multiplied by L^{-1} , where, for Eulerian cradle geometry

$$L = \frac{1}{\sin 2\theta} \quad (2.17)$$

and for the normal beam Weissenberg method

$$L = (\sin^2 2\theta - \sin^2 \chi)^{-1/2} \quad (2.18)$$

Absorption Correction

To correct for the attenuation of the X-ray beam as it passes through the crystal, the intensity must be multiplied by A^{-1} , where

$$A = \frac{1}{V} \int_{\text{crystal}} e^{-\mu(p+q)} d\tau. \quad (2.19)$$

V is the volume of the crystal and p and q are the path lengths for the incident and diffracted beams. μ is the linear absorption coefficient which can be calculated from tabulated values of the mass absorption coefficients (μ_m). If the density of the compound is ρ and the fraction by weight of element i is f_i then

$$\mu = \rho \sum_i f_i \mu_m^i \quad (2.20)$$

where the summation runs over all the elements in the compound. For simple crystal shapes (sphere or cylinder) the integral may be evaluated analytically. Arbitrary crystal shapes require a numerical integration. There are two further corrections that are made to the calculated structure factors during refinement.

Secondary Extinction

A real crystal is considered to be a collection of perfect crystallites, whose orientations vary over a small angular range (mosaic spread). The incident intensity seen by one of these crystallites deep inside the crystal is reduced due to diffraction by similarly aligned crystallites that encounter the beam first. The correction for this effect has been calculated by Zacharisen (1963) and may be applied, according to Larson (1967), using

$$F_C^* = F_C (1 + g\beta(2\theta)F_C^2)^{-1/2}. \quad (2.21)$$

$\beta(2\theta)$ is a factor that represents the variation of secondary ex-

tinction with scattering angle and can be calculated according to Zacharisen. The parameter g is a measure of the extent of the extinction and is a variable in the least squares refinement.

Thermal Motion

The normal atomic scattering factors are calculated on the basis of stationary atoms, but the atoms in crystals are always vibrating about their mean positions, the magnitude of vibration being dependent on temperature. The effect of this thermal motion is to spread the electron clouds over a larger volume and thus to cause the scattering power of an atom to be reduced. In calculating the structure factors the normal atomic scattering factors are replaced by

$$f' = f e^{-B(\sin^2\theta)/\lambda^2} \quad (2.22)$$

B is known as the temperature factor and is proportional to the mean squared amplitude of motion (\bar{u}^2),

$$B = 8\pi^2 \bar{u}^2 \quad (2.23)$$

The above equations assume that the atomic motion is spherically symmetric (isotropic), but in most cases the anisotropy of the arrangement of the surrounding atoms means that \bar{u}^2 varies with direction. Only those displacements perpendicular to the plane of reflection will affect the intensity, so an anisotropic temperature factor must be a function of the Miller indices of this plane. For anisotropic atomic motion equation (2.22) will have the form

$$\exp-(B_{11}h^2 + B_{22}k^2 + B_{33}l^2 + B_{12}hk + B_{13}hl + B_{23}kl).$$

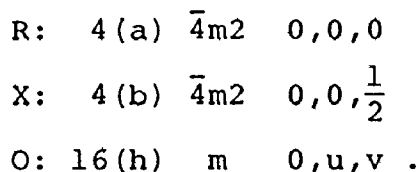
The B's are treated as adjustable parameters in the least squares refinement.

CHAPTER 3

REFINEMENT OF THE CRYSTAL STRUCTURE OF THE COMPOUNDS RXO_4 (R = Tb, Dy; X = As, V) at 300°K

Introduction

These rare earth vanadates and arsenates crystallize with a zircon-type structure conforming to the space group $I4_1/am\bar{d}$ (Wyckoff, 1965). With the origin chosen at $\bar{4}m2$ the atoms occupy the following positions:



Recently these structures have been refined using neutron powder diffraction data (Schafer and Will 1971, Fuess and Kallel 1972). While neutron diffraction is more sensitive to the atomic coordinates of the oxygen atoms, it has not been successfully employed to detect the low temperature crystallographic phase transitions in these compounds (Will and Schafer 1971). This is due to the limited angular resolution available with neutron diffractometers. Since a study of these low temperature phases requires the use of X-ray diffraction techniques, it was decided to undertake a refinement of the room temperature structures using the same technique.

Refinement of Structures

Details of the crystals used in the room temperature structure determination are given in Tables 3.1a-3.1d. In each case the crystal was mounted onto a syntex P1 diffractometer using a Mo K α X-ray source and a graphite crystal monochromator ($2\theta = 12^\circ$). The diffraction angles for 15 reflections with 2θ less than 25 degrees were refined to give the cell dimensions (Tables 3.1a-3.1d).

The intensities were measured using a θ - 2θ scan with variable scan rate. The rate depended upon the maximum counting rate in the intensity profile. The scan rate, in degrees 2θ per minute, varied from $4^\circ/\text{min}$ to $24^\circ/\text{min}$. The background counting rate was measured on both sides of the reflection so that an interpolated background correction could be made. Those reflections whose integrated intensity, after correction for background, was negative were deleted. The range of 2θ over which data was collected may be found in Tables 3.1a-3.1d. Using the computer programmes in the X-ray 71 programme series the intensities were corrected for polarisation and the Lorentz effect. An absorption correction was calculated with the programme Absorp written by R. F. Stewart. After the absorption corrections had been applied symmetry related reflections were averaged.

Refinements of the structures were carried out using a full matrix least squares programme (Cudls) written by J. S. Stevens. The atomic scattering factors for Tb, Tb³⁺, Dy, Dy³⁺,

v^{5+} and As were those tabulated by Cromer and Waber (1964). Atomic scattering factors for O^{--} were those evaluated by Tokonami (1965). The initial oxygen parameters were set at $u = 0.18$ and $v = 0.32$, the values obtained from the neutron powder diffraction studies. When the oxygen positional parameters and the isotropic temperature factors had stabilised, the temperature factors were allowed to become anisotropic. Throughout, an adjustable parameter was refined to correct for the effects of secondary extinction (Larson 1967). In the final few cycles of refinement a weighting function of the following form was used

$$1/w = (A + B|F_o| + C|F_o|^2). \quad (3.1)$$

The weighting scheme was chosen to make the variation in $w\Delta^2$ ($\Delta = |F_c| - |F_o|$) independent of F_o . This method (Cruickshank et al. 1961) assumes that the Δ 's are due to random errors of measurement. A fourth term

$$D \left| \frac{\sigma(F_c)}{|F_c|} \right|^2$$

was added to the weighting scheme so that the very weak reflections were not over weighted. D was chosen such that for $I = 3\sigma(I)$ this last term equalled the sum of the other terms. The inclusion of weights in the least squares algorithm means that the quantity to be minimised is

$$R_w = \sum_i \omega_i \Delta_i^2 / \sum_i \omega_i |F_o|^2. \quad (3.2)$$

The refinement was terminated when the parameter shifts were all less than one tenth of their standard deviations. The final residuals are given in Tables 3.1a-3.1d. The final atomic coordinates are presented in Tables 3.2a-3.2d, the interatomic distances and angles in Tables 3.3a-3.3d and the observed and calculated structure factors in Tables 3.4a-3.4d.

Discussion

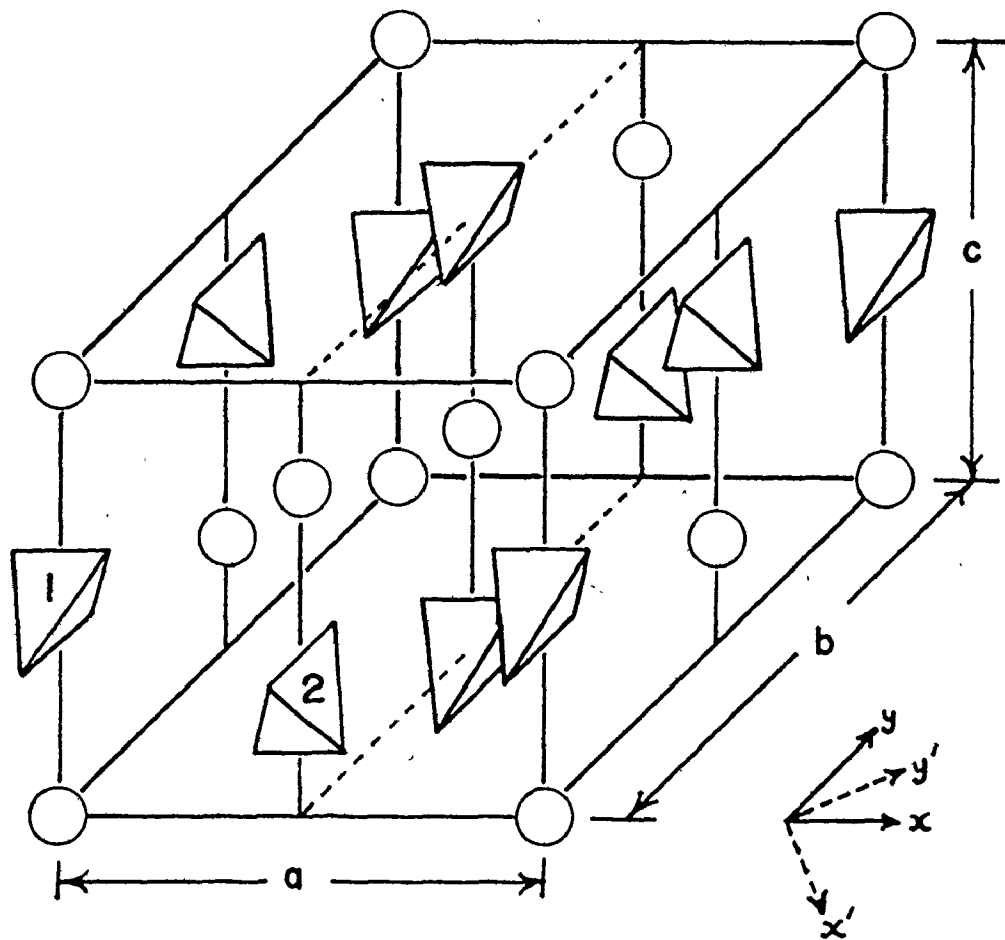
The crystal structure, shown in Fig. 3.1, of the rare earth arsenates and vanadates consist of slightly distorted VO_4^{3-} or AsO_4^{3-} tetrahedra with rare earth ions between the tetrahedra.

The V-O distances, within the tetrahedra of the vanadates, agrees, within experimental error, with the mean value of $1.721(12) \text{ \AA}$ determined from 22 accurately refined vanadate structures (Shannon and Calvo 1973). The As-O distances in the arsenates agrees well with the value of $1.681(2) \text{ \AA}$ obtained in a recent determination of the structure of LuAsO_4 (Lohmüller et al. 1973). LuAsO_4 also crystallizes in the zircon structure.

The oxygen positional parameters, (u,v) for the vanadates, agree well with those calculated by Baglio and Sovers (1971). Their calculation consisted of minimising the lattice energy, of rare earth vanadates with the zircon structure, as a function of the oxygen parameters. They found the values of u and v obtained from the minimisation consistent with the assumption that the VO_4^{3-} tetrahedron is identical in all the

Fig. 3.1

Schematic representation of the tetragonal zircon structure.



$\text{AsO}_4, \text{VO}_4$



Dy, Tb

rare earth vanadates. Using this assumption they obtain the following expressions for the variation of u and v with atomic number (Z).

$$u = 0.09841 + 1.905 \times 10^{-3} Z - 9.066 \times 10^{-6} Z^2, \quad (3.3)$$

$$v = 0.42278 - 2.421 \times 10^{-3} Z + 14.491 \times 10^{-6} Z^2.$$

For DyVO_4 and TbVO_4 these equations give

$$\begin{array}{l} \text{DyVO}_4 : u = 0.1846 \quad ; \quad v = 0.3261 \\ \quad \quad \quad (0.184) \quad ; \quad \quad (0.326) \\ \text{TbVO}_4 \text{ " } u = 0.1839 \quad ; \quad v = 0.3266 \\ \quad \quad \quad (0.183) \quad \quad \quad (0.327) . \end{array}$$

The values in parentheses, under the calculated values, are the experimental results obtained in this work. The assumption of unchanging VO_4^{3-} geometry is supported by this determination of this geometry in DyVO_4 and TbVO_4 . The geometry is identical, within experimental error, to that found in NdVO_4 by Baglio and Sovers (1971).

In the case of the arsenates, the AsO_4^{3-} tetrahedron is the same for DyAsO_4 and TbAsO_4 , and is very close to that found in LuAsO_4 (Lohmüller et al. 1973). A similar set of equations to (3.3) should also be a valid source of oxygen parameters in the case of the rare earth arsenates. Following Baglio and Sovers, and using the data from DyAsO_4 , TbAsO_4 and LuAsO_4 , we obtain

$$\begin{aligned}
 u &= 0.151 + 4.6 \times 10^{-4} z \\
 v &= 0.367 - 6.2 \times 10^{-4} z
 \end{aligned}
 \tag{3.4}$$

The temperature factors for the heavy atoms are expected to be unreliable. This is a result of the large linear absorption coefficients and the experimental error in measuring the size of the crystal. The uncertainty is expected to be largest for U_{33} as the largest dimension of the crystal is along the c axis.

The Crystal Field at the Rare Earth Site

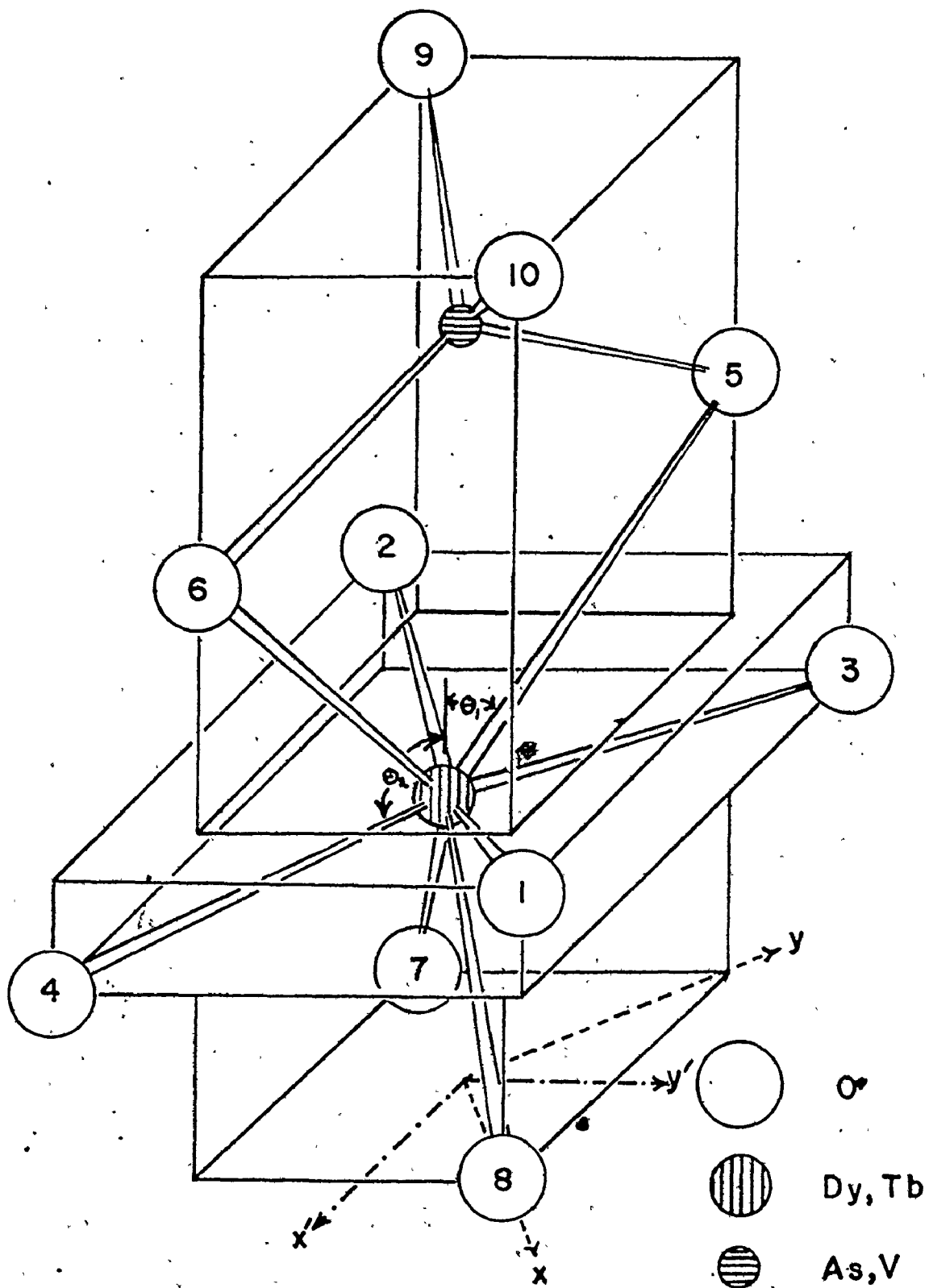
The rare earth site, in these compounds, is surrounded by a dodecahedron of oxygen atoms, as shown in Fig. 3.2. This arrangement is very important in determining why there is a low temperature phase transition in these materials. It is the cage of oxygen atoms that determines the crystal field at the site. The rare earth site has point symmetry D_{2d} so we may write the crystal field Hamiltonian, in operator equivalent form, as (Brecher et al 1964)

$$\begin{aligned}
 H_c &= A_2^O \langle r^2 \rangle \langle J || \alpha || J \rangle O_2^O + \langle J || \beta || J \rangle \langle r^4 \rangle (A_4^O O_4^O + A_4^4 O_4^4) \\
 &+ \langle J || \gamma || J \rangle \langle r^6 \rangle (A_6^O O_6^O + A_6^4 O_6^4)
 \end{aligned}
 \tag{3.5}$$

where A_m^n is a crystal field parameter, $\langle r^n \rangle$ is a radial expectation value for the 4f electrons in the rare earth ion (Freeman and Watson 1962), O_m^n is an operator equivalent (Hutchings 1964) and the $\langle J || \alpha || J \rangle$ etc. are reduced matrix elements characteristic of the particular ion under considera-

Fig. 3.2

Environment of the rare earth ion in the
zircon structure.



tion (Hutchings 1964). The crystal field parameters are determined by fitting equation (3.5) to energy levels of the ions. These energies are usually obtained by optical spectroscopy.

For the rare earth phosphates, arsenates and vanadates the most important features of the crystal field are, that A_4^4 is very large and A_2^0 is positive for the phosphates but negative for the arsenates and vanadates. It is this second feature that provides the reason why the phosphates do not undergo a Jahn-Teller transition. A positive value of A_2^0 results in the lowest level of the ion being an approximate eigenstate of the operator J_z with J_z taking on its maximum value J . A negative value favours the lowest level being an eigenstate of J_x with $J_x = J$, i.e. $|J_x = J\rangle$. Because of the four fold symmetry the states $|J_x = -J\rangle$, $|J_y = J\rangle$ and $|J_y = -J\rangle$ must also be of low energy, this results in the ground state being an approximately degenerate quartet. This degeneracy is required if there is to be a Jahn-Teller coupling to lattice distortions. The term involving A_4^4 determines the direction in the basal plane along which the moment, associated with the above states, will lie. For Dy^{3+} x and y correspond to the cell axes a and b , whereas for Tb^{3+} $\langle J || \beta || J \rangle$ is of opposite sign. This results in x and y lying 45° to a and b .

We can describe the crystal field in purely electrostatic terms by placing point charges, corresponding to the O^{2-} ions around the metal ion in a dodecahedral arrangement. This arrangement can be characterised by two angles θ_1 and θ_2 . These

are shown in Fig. 3.2. Brecher et al. (1968) have obtained expressions relating the parameters A_n^m to θ_1 and θ_2 , using the assumption that the O^{2-} charges are all at the same distance R from the rare earth ion. They take this distance to be the radius of the rare earth ion. The expressions they obtain are

$$\frac{R^2 \left[\frac{4}{35} \sqrt{70} A_4^4 + 8A_4^0 \right]}{2A_2^0} = \frac{5(\cos^2(\theta_1) + \cos^2(\theta_2)) - 8}{6(\cos^2\theta_1 + \cos^2\theta_2) - 4} \quad (3.6)$$

and

$$\frac{R^4 \left[\frac{8}{21} \sqrt{14} A_6^4 + 48A_6^0 \right]}{2A_2^0} = \frac{63(\cos^4\theta_1 + \cos^4\theta_2) - 63(\cos^2\theta_1 + \cos^2\theta_2) + 12}{24(\cos^2\theta_1 + \cos^2\theta_2) - 16}$$

where R is the radius of the rare earth ion. From these we see that the condition for A_2^0 to change sign is

$$(\cos^2\theta_1 + \cos^2\theta_2) < \frac{2}{3}. \quad (3.7)$$

For a pure dodecahedron $\theta_1 = 36.9^\circ$ and $\theta_2 = 110.6^\circ$. If small distortions from this are going to satisfy (3.7) then θ_1 must increase and θ_2 must decrease, i.e. the dodecahedron must become oblate. For the phosphates the dodecahedron is almost pure (Brecher et al. 1968) whereas for the vanadates and the arsenates it is slightly oblate. Because of the assumption that the O^{2-} charges are equidistant from the rare earth ion, the values of θ_1 and θ_2 obtained from X-ray data will not equal those obtained from Brecher's point charge calculation. However, Brecher finds that there is a direct correlation between the two. The dodecahedron of the O^{2-} ions in the vanadates,

as determined from X-ray data is more oblate than in the phosphates. For yttrium vanadate, Brecher's crystal field analysis gives the values $\theta_1 = 38.3^\circ$ and $\theta_2 = 94.7^\circ$. The corresponding values obtained from X-ray data are $\theta_1 = 32.5^\circ$ and $\theta_2 = 102.2^\circ$. Tables 3.3a-3.3d permit the calculation of the X-ray values of these angles. For the compounds studied here, these are

	<u>θ_1</u>	<u>θ_2</u>
DyVO ₄ :	32.6	101.9
DyAsO ₄ :	31.7	102.2
TbVO ₄ :	32.4	102.1
TbAsO ₄ :	31.8	102.2

The values are almost identical, indicating that the crystal field at the rare earth site is almost the same in each compound. We also notice the values compare favourably with those in yttrium vanadate, where the point charge distribution is known to correspond to an oblate dodecahedron.

The X-ray data is consistent with the idea that an oblate dodecahedron leads to a negative A_2^0 and this is responsible for the phase transition.

Table 3.1a
Crystal data for DyVO₄ at 300°K

Lattice parameters: $a = b = 7.151(2) \text{ \AA}$;
 $c = 6.293(3) \text{ \AA}$; $\alpha = \beta = \gamma = 90^\circ$

Faces bounding the crystal and the distance (d) along the face normal to a point inside the crystal.	<u>Crystal face</u>	<u>d mm.</u>
	(1, 0, 0)	0.015 (8)
	($\bar{1}$, 0, 0)	0.020 (8)
	(0, 1, 0)	0.020 (8)
	(0, $\bar{1}$, 0)	0.020 (8)
	(0, 0, 1)	0.090 (8)

Linear absorption coefficient: $\mu = 245.9 \text{ cm}^{-1}$

Range of data collection: $2\theta < 65^\circ$

Total number of reflections measured: 165

Number of unique reflections: 93

Weighting function: $\frac{1}{w} = 14.25 - 0.391 |F_0| + 0.035 |F_0|^2 + 425.0 \frac{\sigma(F_0)^2}{|F_0|}$

Secondary extinction parameter: $g = 2.55 \times 10^{-6}$

Final residuals: $R_w = 0.041$; $R = 0.040$

* Throughout this work standard deviations are given in parentheses.

Table 3.1bCrystal data for DyAsO₄ at 300°K

Lattice parameters: $a = b = 7.063(4) \text{ \AA}$;
 $c = 6.304(3) \text{ \AA}$ $\alpha = \beta = \gamma = 90^\circ$

Faces bounding the crystal and the distance (d) along the face normal to a point inside the crystal.	<u>Crystal face</u>	<u>d mm.</u>
	(1,0,0)	0.034(8)
	($\bar{1}$,0,0)	0.034(8)
	(0,1,0)	0.034(8)
	(0, $\bar{1}$,0)	0.034(8)
	(0,0,1)	0.187(8)
	(0,0, $\bar{1}$)	0.187(8)

Linear absorption coefficient: $\mu = 352.9 \text{ cm}^{-1}$

Range of data collection: $2\theta < 70^\circ$

Total number of reflections measured: 434

Number of unique reflections : 185

Weighting function: $\frac{1}{w} = 5.45 - 0.206|F_0| + 0.0050|F_0|^2 + 100.0 \frac{\sigma(F_0)^2}{|F_0|}$

Secondary extinction parameter: $g = 2.29 \times 10^{-6}$

Final residuals: $R_w = 0.059$; $R = 0.051^*$

Table 3.1cCrystal data for TbVO₄ at 300°K

Lattice parameters: $a = b = 7.176(3) \text{ \AA} ;$
 $c = 6.323(3) \text{ \AA} ; \alpha = \beta = \gamma = 90^\circ$

Faces bounding the crystal and the distance (d) along the face normal to a point inside the crystal.	<u>Crystal face</u>	<u>d mm.</u>
	(1,0,0)	0.085(8)
	($\bar{1}$,0,0)	0.085(8)
	(0,1,0)	0.050(8)
	(0, $\bar{1}$,0)	0.050(8)
	(0,0,1)	0.125(8)
	(0,0, $\bar{1}$)	0.125(8)

Linear absorption coefficient: $\mu_r = 238.7 \text{ cm}^{-1}$

Range of data collection: $2\theta < 65^\circ$

Total number of reflections measured: 884

Number of unique reflections: 158

Weighting function: $\frac{1}{w} = 3.92 + 0.0314 |F_0| + 0.0031 |F_0|^2 + 36.0 \frac{\sigma(F_0)^2}{|F_0|}$

Secondary extinction parameter: $g = 5.45 \times 10^{-6}$

Final residuals: $R_w = 0.067 ; R = 0.055$

Table 3.1d

Crystal data for TbAsO₄ at 300°K

Lattice parameters: $a = b = 7.075(3) \text{ \AA}$;
 $c = 6.316(2) \text{ \AA}$; $\alpha = \beta = \gamma = 90^\circ$

Faces bounding the crystal and the distance (d) along the face normal to a point inside the crystal	<u>Crystal face</u>	<u>d mm.</u>
	(1,0,0)	0.050(8)
	($\bar{1}$,0,0)	0.050(8)
	(0,1,0)	0.050(8)
	(0, $\bar{1}$,0)	0.050(8)
	(0,0,1)	0.285(8)
	(0,0, $\bar{1}$)	0.285(8)

Linear absorption coefficient: $\mu = 304.8 \text{ cm}^{-1}$

Range of data collection: $2\theta < 65^\circ$

Total number of reflections measured: 526

Number of unique reflections: 142

Weighting function: $\frac{1}{w} = 10.20 - 0.299|F_0| + 0.0051|F_0|^2 + 160.0 \frac{\sigma(F_0)^2}{|F_0|}$

Secondary extinction parameter: $g = 3.05 \times 10^{-6}$

Final residuals: $R_w = 0.061$; $R = 0.054$

Table 3.2a

Final atomic parameters for DyVO_4 at 300°K

Atom	x	y	z	U_{11}	U_{22}	U_{33}	U_{23}
Dy ³⁺	0.0	0.0	0.0	24(10)	24(10)	31(11)	0
V ⁵⁺	0.0	0.0	0.5	10(37)	10(37)	109(34)	0
O ²⁻	0.0	0.184(1)	0.326(1)	88(48)	72(46)	40(56)	-9(23)

Table 3.2b

Final Atomic parameters for DyAsO_4 at 300°K

Atom	x	y	z	U_{11}	U_{22}	U_{33}	U_{23}
Dy	0.0	0.0	0.0	94(9)	94(9)	28(6)	0
As	0.0	0.0	0.5	100(13)	100(13)	29(11)	0
O	0.0	0.181(1)	0.327(1)	193(23)	101(19)	57(18)	14(15)

*The expression used to calculate the thermal effect was

$$\exp(-2\pi^2 [a^2 U_{11} h^2 + \dots + 2b^*c^* U_{23} k^2 + \dots]).$$

Table 3.2cFinal atomic parameters for TbVO₄ at 300°K

Atom	x	y	z	U ₁₁	U ₂₂	U ₃₃	U ₂₃
Tb ³⁺	0.0	0.0	0.0	66(14)	66(14)	111(8)	0
V ⁵⁺	0.0	0.0	0.5	44(28)	44(28)	114(21)	0
O ²⁻	0.0	0.183(1)	0.327(1)	126(36)	77(30)	126(30)	-3(23)

Table 3.2dFinal atomic parameters for TbAsO₄ at 300°K

Atom	x	y	z	U ₁₁	U ₂₂	U ₃₃	U ₂₃
Tb	0.0	0.0	0.0	42(13)	42(13)	58(7)	0
As	0.0	0.0	0.5	47(21)	47(21)	76(14)	0
O	0.0	0.181(1)	0.327(1)	121(28)	68(28)	73(24)	18(20)

Table 3.3a
Bond lengths and angles for DyVO₄ at 300°K

Atoms	Distances (Å)	Atoms	Angles (°)
V-0	1.710(9)	0(1)*-Dy-0(2)	156.1(3)
Dy-0(1)	2.313(10)	0(1)-Dy-0(3)	92.5(2)
Dy-0(5)	2.435(9)	0(5)-Dy-0(6)	65.2(3)
0(5)-0(6)	2.625(14)	0(5)-Dy-0(7)	135.2(2)
0(3)-0(5)	2.702(12)	0(5)-V-0(6)	100.3(4)
0(5)-0(9)	2.871(11)	0(5)-V-0(9)	114.2(3)
0(1)-0(5)	3.053(12)		
0(1)-0(3)	3.340(10)		

Table 3.3b
Bond lengths and angles for DyAsO₄ at 300°K

Atoms	Distances (Å)	Atoms	Angles (°)
As-0	1.676(5)	0(1)-Dy-0(2)	155.6(2)
Dy-0(1)	2.309(5)	0(1)-Dy-0(3)	92.6(1)
Dy-0(5)	2.426(5)	0(5)-Dy-0(6)	63.4(2)
0(5)-0(6)	2.549(8)	0(5)-Dy-0(7)	136.4(1)
0(3)-0(5)	2.735(8)	0(5)-As-0(6)	99.0(3)
0(5)-0(9)	2.825(7)	0(5)-As-0(9)	114.9(2)
0(1)-0(5)	3.033(5)		
0(1)-0(3)	3.338(6)		

*The label on the oxygen atoms in Table 3.3a-d refer to that used in Fig. 3.2.

Table 3.3c
Bond lengths and angles for TbVO₄ at 300°K

Atoms	Distances (Å)	Atoms	Angles (°)
V-0	1.707(7)	O(1)-Tb-0(2)	155.9(2)
Tb-0(1)	2.330(6)	O(1)-Tb-0(3)	92.5(2)
Tb-0(5)	2.449(6)	O(5)-Tb-0(6)	64.6(2)
O(5)-O(6)	2.622(10)	O(5)-Tb-0(7)	135.5(2)
O(3)-O(5)	2.733(10)	O(5)-V-0(6)	100.3(3)
O(5)-O(9)	2.867(7)	O(5)-V-0(9)	114.2(3)
O(1)-O(5)	3.068(9)		
O(1)-O(3)	3.367(7)		

Table 3.3d
Bond lengths and angles for TbAsO₄ at 300°K

Atoms	Distances (Å)	Atoms	Angles (°)
As-0	1.681(4)	O(1)-Tb-0(2)	155.6(2)
Tb-0(1)	2.311(7)	O(1)-Tb-0(3)	92.6(2)
Tb-0(5)	2.431(6)	O(5)-Tb-0(6)	63.5(2)
O(5)-O(6)	2.558(10)	O(5)-Tb-0(7)	136.3(2)
O(3)-O(5)	2.738(9)	O(5)-As-0(6)	99.1(3)
O(5)-O(9)	2.833(8)	O(5)-As-0(9)	114.9(2)
O(1)-O(5)	3.038(9)		
O(1)-O(3)	3.340(7)		

Table 3.4a

OBSERVED AND CALCULATED STRUCTURE FACTORS OF DYSPROSIUM VANADATE 300 DEG K

H	K	L	FO	FC	H	K	L	FO	FC	H	K	L	FO	FC	H	K	L	FO	FC
0	2	0	173	160	1	3	4	86	7	1	0	2	143	137	1	0	2	46	46
0	4	0	120	102	1	5	4	69	61	1	2	4	148	139	1	0	4	48	48
0	4	2	177	159	1	5	4	72	68	1	2	4	118	116	1	0	4	50	50
0	6	0	179	159	1	5	4	107	105	1	4	4	117	116	1	0	6	8	8
1	1	1	96	88	1	5	5	159	152	1	4	5	154	152	1	1	1	152	152
1	1	1	77	73	1	5	5	161	157	1	4	5	177	175	1	1	1	173	173
1	1	1	82	78	1	5	5	133	129	1	4	5	154	152	1	1	1	171	171
1	1	1	95	92	1	5	5	223	219	1	4	5	180	178	1	1	1	180	180
1	1	1	110	107	1	5	5	154	152	1	4	5	154	152	1	1	1	174	174
2	2	2	116	112	1	5	5	130	127	1	4	5	154	152	1	1	1	175	175
2	2	2	161	157	1	5	5	101	99	1	4	5	154	152	1	1	1	144	144
2	2	2	173	169	1	5	5	117	115	1	4	5	154	152	1	1	1	144	144
2	2	2	193	191	1	5	5	140	138	1	4	5	154	152	1	1	1	158	158
2	2	2	209	207	1	5	5	151	149	1	4	5	154	152	1	1	1	180	180
2	2	2	220	218	1	5	5	151	149	1	4	5	154	152	1	1	1	180	180
3	3	3	189	187	1	5	6	111	109	1	4	6	154	152	1	1	1	203	203
3	3	3	189	187	1	5	6	111	109	1	4	6	154	152	1	1	1	203	203

CHAPTER 4

THE LOW TEMPERATURE DIFFRACTOMETER

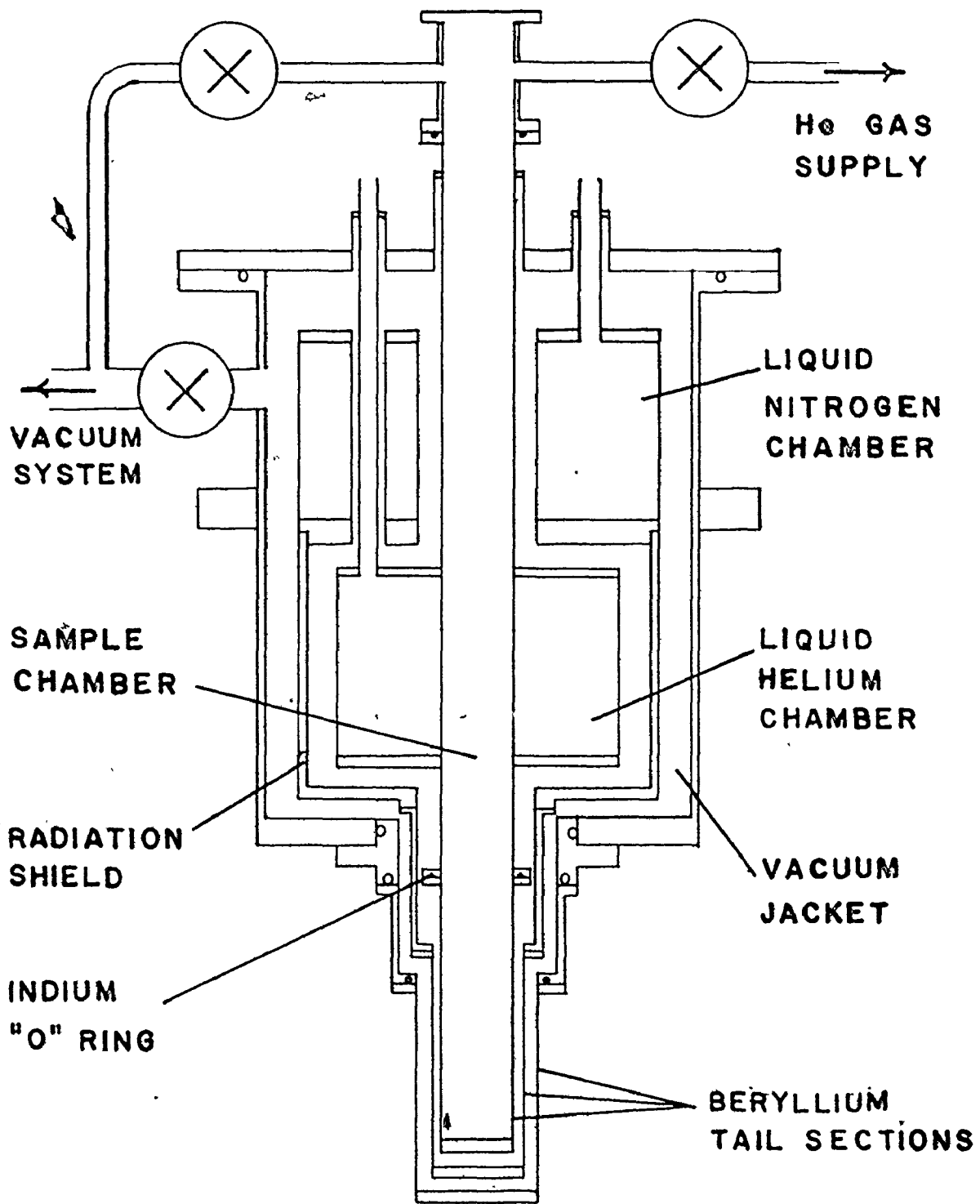
A manually operated diffractometer was designed and constructed to determine the low temperature crystal structures. The geometry of the instrument is that of a normal beam Weissenberg camera, with provision for film or scintillation counter direction. The crystal is mounted inside a cryostat. By using different cryogenic liquids and a temperature control unit, the diffractometer may be used to determine crystal structures from room temperature down to 6°K. In the following sections the design of the various components of the instrument and the alignment procedure are described in considerable detail. It is hoped that this section might be of use to future users of the instrument.

The Cryostat

The dewar used is of conventional design. A schematic diagram of its construction is shown in Fig. 4.1. With the exception of the outer shell and the beryllium tail sections, the construction was carried out in the McMaster University Instrument Machine Shop under the supervision of Mr. S. Kocsis. The aluminium shell for the dewar is from an Oxford Instruments powder diffraction dewar and the tail section was fabricated by Grant & Kemper Ltd., San Diego, Cal.

Fig. 4.1

Sectional drawing of the cryostat used
with the low temperature diffractometer.



To allow the passage of X-rays to and from the sample, without severe attenuation, it is necessary that the tail sections of the dewar be thin-walled and made of a material with a low electron density. Beryllium being rigid and having a low atomic number is an ideal material. However, the fabrication of beryllium products is costly due to its high toxicity. Beryllium is also quite brittle, so it is unadvisable to have the flanges of the tail sections made of beryllium. These are made from stainless steel and brazed to the beryllium. The brazes are necessary because the joints must remain vacuum tight through the many thermal shocks involved in cycling it between 4.2°K and room temperature.

Apart from where it is otherwise indicated the material used in the construction of the inner parts of the dewar is stainless steel. Wherever possible thin-wall (.010") tubing or sheet was used, to minimize thermal conduction.

One of the three ports to the liquid nitrogen chamber houses a probe connected to a liquid level controller. This unit is used to keep the nitrogen vessel full during lengthy experiments. A helium liquid level indicator probe is located in one of the helium chamber ports. This was used as an aid during transfer and for monitoring the liquid level.

In normal operation with the sample held at 6°K, liquid helium need only be transferred every 14 hours.

Sample Holder

The sample holder construction is shown in Fig. 4.2. It was designed so that small changes in sample orientation could be made quickly and easily. This is a necessary feature because, on cooling from room temperature, differential thermal contractions can cause quite large shifts in sample position. With the design used the crystallographic axis aligned along the sample holder can be rotated about two perpendicular axes, referred to as the goniometer axes. The mechanism is rather like a ball and socket joint. The ball is rigidly attached to the sample holder post and sits in a truncated conical cavity in a teflon cylinder. This can be made to rotate about the ball using the adjusting screws, which work against the spring loaded pins.

A heater is wound on the copper section of the post to allow the sample temperature to be raised. The temperature is measured by a carbon resistance thermometer, located as close to the sample as possible. Both the heater and the thermometer are connected to a proportional temperature control unit. During an experiment the sample chamber of the dewar is filled with helium exchange gas. This aids thermal conduction between the sample and the liquid helium bath and decreases the thermal time constant of the system.

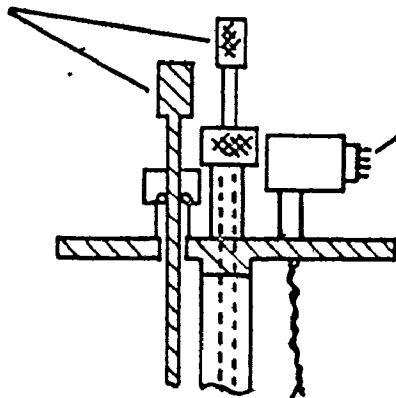
The crystal under study is mounted in a fine silica glass capillary. A fine copper wire (44 awg.) is also placed in the capillary so that its end is about 1/16" from the

Fig. 4.2

Sectional drawing of the sample holder
used at low temperatures.

ADJUSTING
SCREWS

ELECTRICAL
FEED THROUGH



THERMOMETER

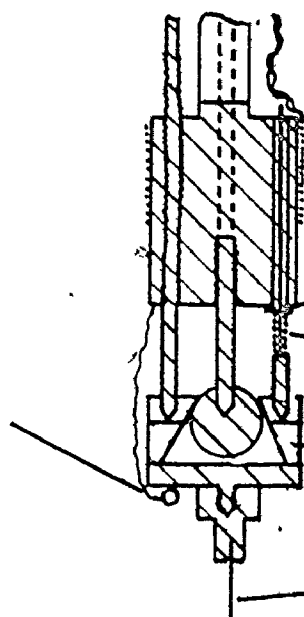
HEATER

TEFLON SLEEVE

COMPRESSION
SPRING

TEFLON

SAMPLE



crystal. The purpose of the wire is to help position the crystal in the X-ray beam (see crystal alignment section). The capillary is then glued into a brass plug using G.E. 7031 varnish, and the plug is screwed into the sample plate.

Mounting Table

During an experiment the dewar is held on a table that sits on the X-ray generator. The essential details of the table are shown in Fig. 4.3.

The function of the assembly on top of the main table is two fold. First it enables the sample and dewar to be rotated about an axis perpendicular to the incident X-ray beam, second it allows the centering of the sample on this rotation axis.

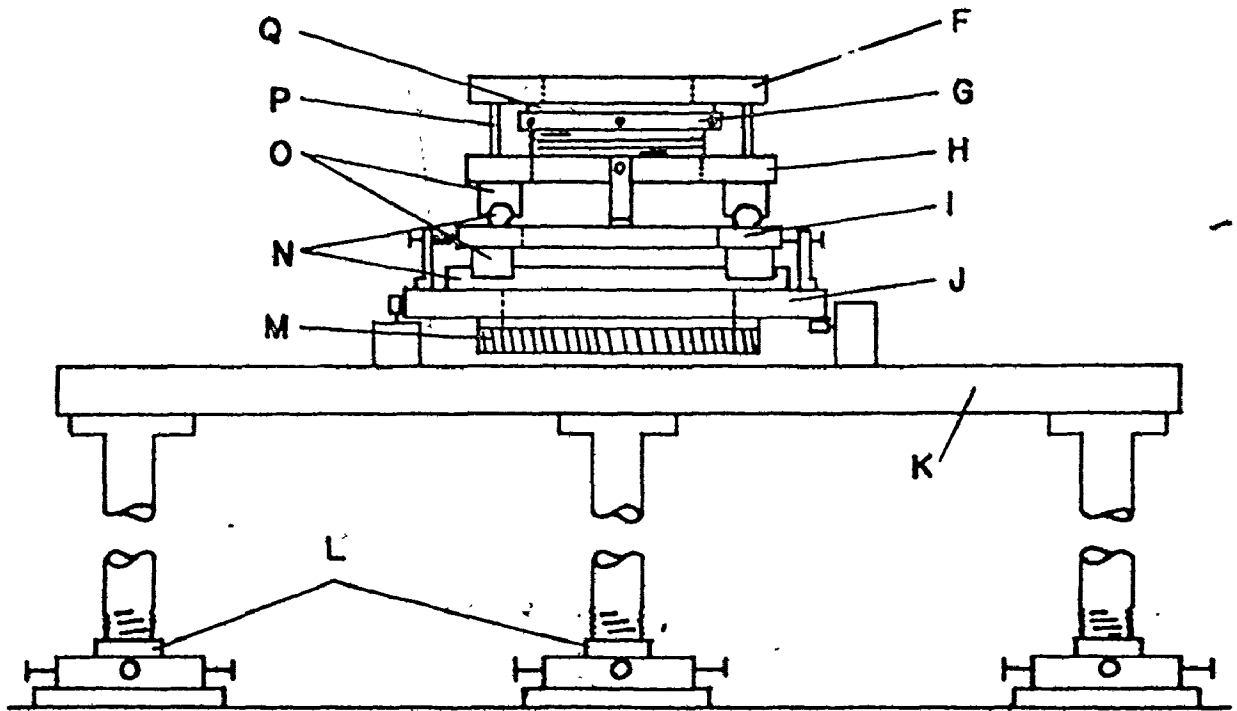
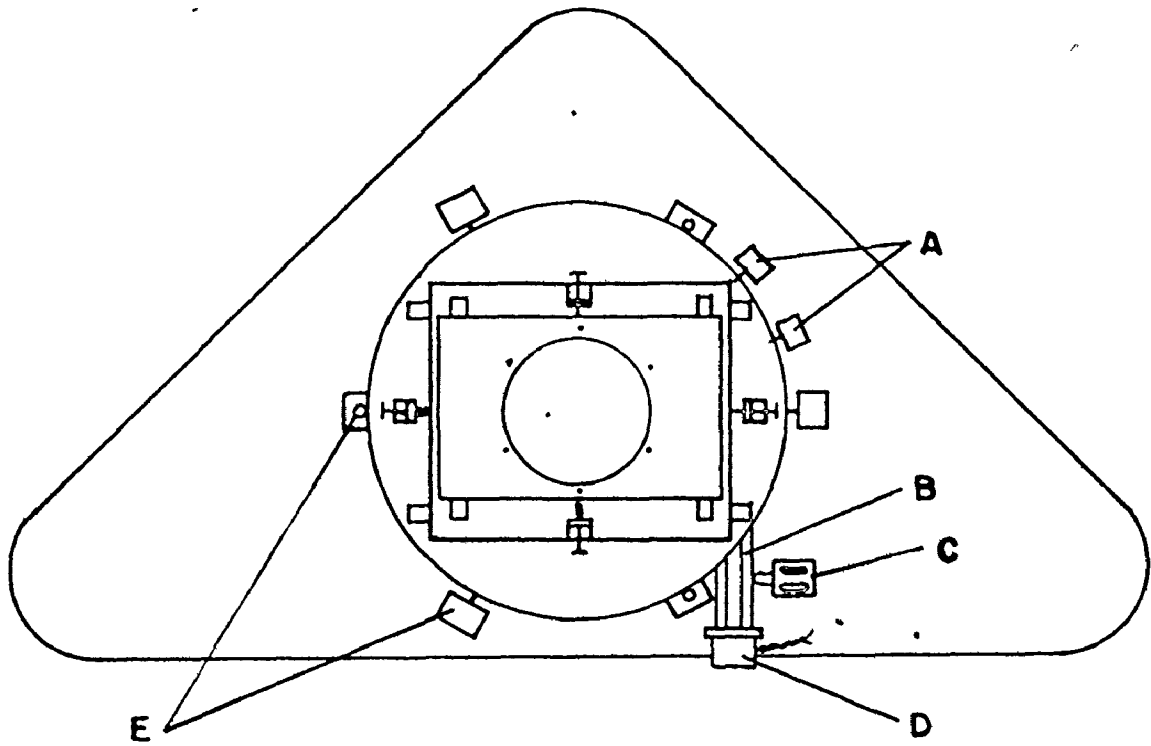
The sample and dewar are rotated by means of the turntable which is supported on the main table by six bearings. The turntable can be turned either by a synchronous motor or manually, by disengaging the worm assembly. The motor can drive the turntable both clockwise and counterclockwise at a rate of 1 revolution per 50 minutes. The direction of the travel can be reversed automatically by the two micro-switches. These engage pins which can be placed every 5° around the turntable circumference. The position of the turntable, with respect to some arbitrary origin, can be monitored by a mechanism attached to the worm assembly. This consists of an indexing wheel that is connected to the worm via a gear box. The angular velocity of the index wheel is

Table 4.3

Construction of the mounting table
for the cryostat

Key

A - Microswitches	J - Turntable
B - Worm assembly	K - Main table
C - Clutch	L - Base plates
D - Motor	M - Worm gear
E - Bearings	N - Stainless steel slides
F - Dewar mounting plate	O - Delrin bearing
G - Height adjustment screw	P - Locating pins
H - X table	Q - Teflon washer
I - Y table	



22

ten times that of the worm. The wheel has 36 equally spaced holes around its circumference. As the wheel rotates the holes make and break the circuit between a matched light emitting diode and photo-transistor, resulting in a series of pulses in the transistor circuit. The turntable is geared down from the motor by a factor of 100, hence each pulse corresponds to a turntable rotation of 0.01° . The pulses are counted using a modified electronic calculator. The add or subtract contact is made depending on the direction of travel and the pulses make or break the numeral one contact. The display shows the running total. The zero is reset by pressing the clear button. The rotation of the table corresponds to the coordinate ω of chapter 2.

Stacked on top of the turntable are the X and Y translation tables which are used to position the sample on the rotation axis. The height of the sample along this axis can be adjusted by means of the threaded cylinder mounted on the X table. When making height changes the dewar is prevented from rotating by two locating pins.

The legs of the main table are threaded at the bottom and screw into base plates which may be rotated to allow the table to be leveled. The plates are held in position using four bolts. The bolts are also used to translate the table during alignment.

Detector and Camera

Either a scintillation counter or a film may be used to detect X-rays in this system. Both camera and counter use a Philips horizontal goniometer as their base. The rotation axis of the horizontal goniometer is aligned with that of the mounting table. The camera, when in use, sits on a table that takes the place of the sample holder in the usual use of the instrument. This is held at the correct height by a removable spacer. The design of the camera is basically that of a Weissenberg camera except that it has an exit hole for the X-ray beam.

The counter is mounted on the 2θ table of the horizontal goniometer in a housing (Fig. 4.4) that allows it to be rotated about a horizontal axis. This enables the counter to be set at different values of the coordinate χ of Chapter 2. The 2θ coordinate of the horizontal goniometer corresponds to γ . A collimator or slit can be mounted at the front of the detector housing, and an incident beam collimator is mounted on the horizontal goniometer.

The detection electronics used in conjunction with the scintillation counter is that conventionally used with the horizontal goniometer.

Fig. 4.5 is a photograph of the diffractometer with all of the components present.

Fig. 4.4

The detector housing mounted on the horizontal goniometer.



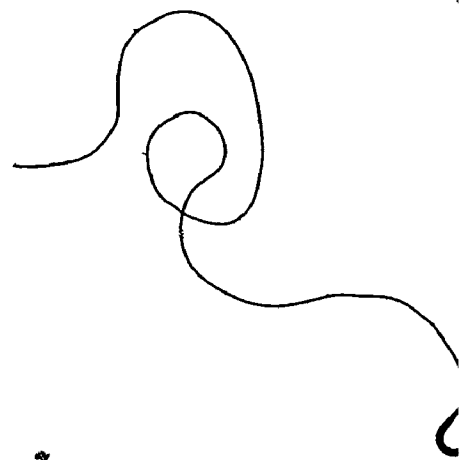
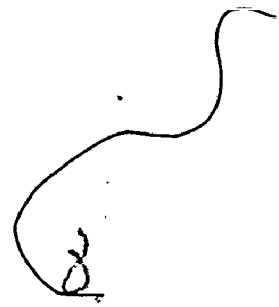
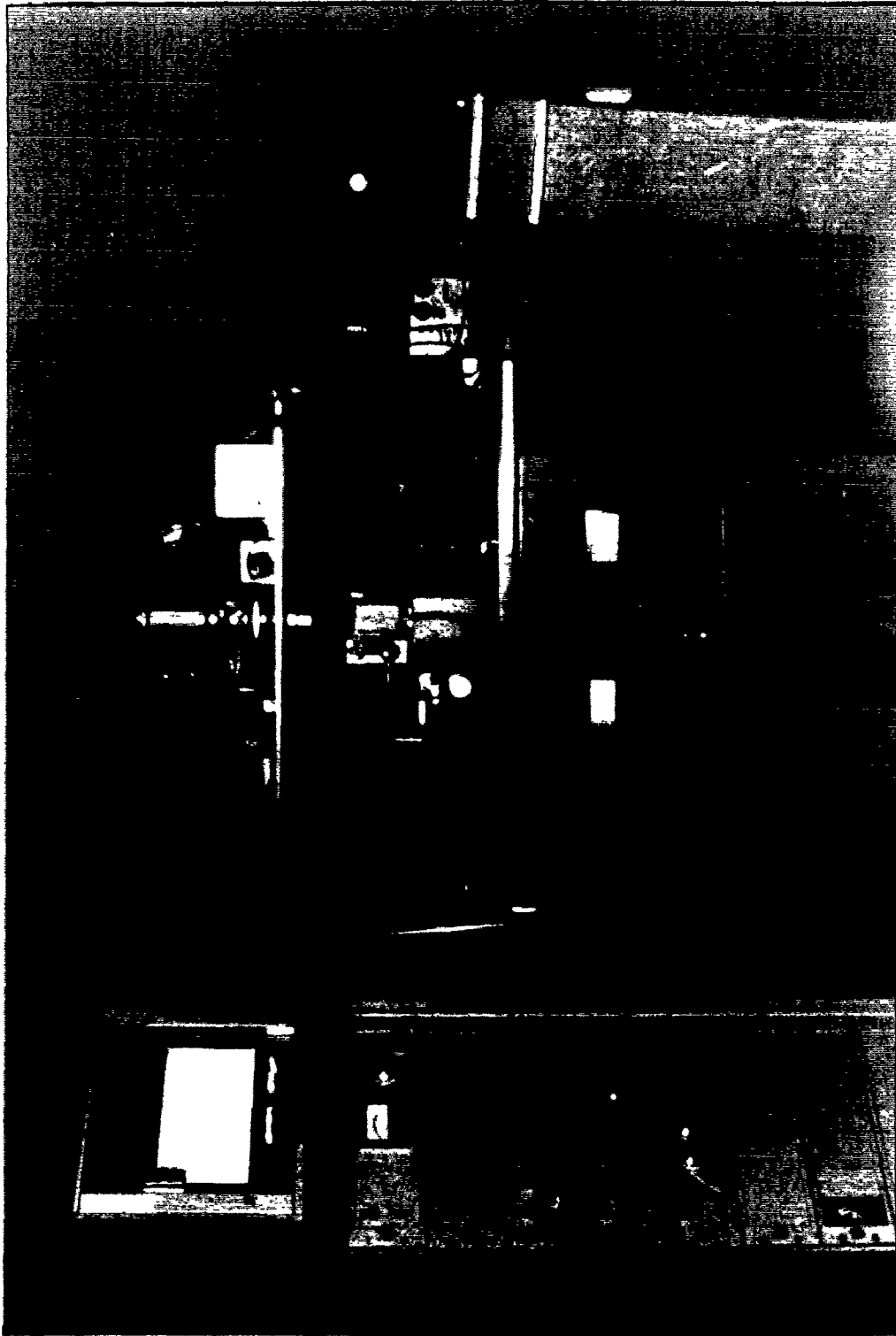


Fig. 4.5

The low temperature diffractometer in use.





Alignment of Diffractometer

The detector assembly was constructed and mounted on the 2θ table so that the χ and γ axes intersect at right angles. With the horizontal goniometer leveled and, following the instruction manual, the X-ray beam is aligned to intersect the γ axis at right angles at the height of the χ axis.

The cryostat table is then fixed on the generator so that the ω axis is roughly colinear with the γ axis. The table is leveled and the dewar mounted. The mounting ring of the dewar is adjusted so that the top flange is level and its height such that the sample is roughly at the level of the X-ray beam. Also the goniometer axes are adjusted to coincide with the axes of the X-Y tables.

In the final stage of alignment a dial indicator is mounted on the detector housing. The "reeler" of the indicator is placed against the tail of the dewar above the beryllium piece. The turntable is rotated and the X-Y tables adjusted until the axis of the dewar coincides with the ω axis. The dewar is then held in position and the detector housing rotated about the γ axis. The base plates of the table are translated until the γ axis is colinear with the ω axis.

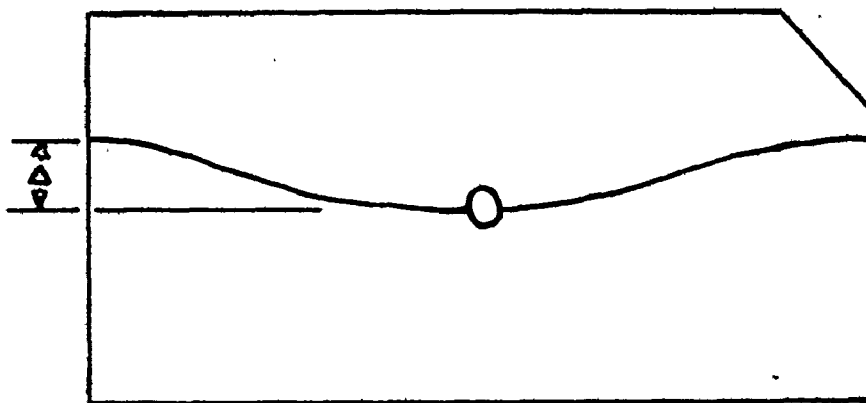
The instrument is then ready for use.

Alignment of Sample

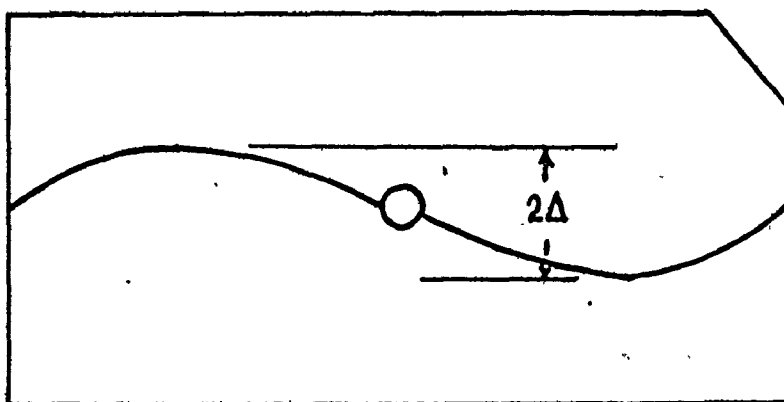
With a sample prepared as described in a previous section the sample holder is placed inside the dewar and the flange

Fig. 4.6

Appearance of zero-layer lines on oscillation photographs of a misaligned crystal.



BACK TO FRONT MISALIGNMENT



SIDE TO SIDE MISALIGNMENT

bolted down. A coarse collimator is used in the incident beam, one that will give a 5 mm. diameter beam at the sample. This beam is observed upon exit from the dewar using a fluorescent screen. By rotating the dewar the shadow of the copper wire is located. Failure to locate the shadow means that the dewar needs to be lowered. Once the shadow is located the height of the dewar is changed until the end of the wire is at the centre of the beam. Next the X-Y tables are adjusted until the end of the wire does not move upon rotation of the dewar. Finally the dewar is raised the distance between the end of the wire and the centre of the crystal.

With the crystal centered in the X-ray beam, the next step is the alignment of the correct crystallographic axis along the rotation axis. The initial alignment is done photographically using an oscillation photograph. The dewar is oscillated 15° with one of the goniometer axes along the X-ray beam at the centre of the oscillation period. Unfiltered radiation is used and a fine collimator replaces the one used previously. Typical exposure times are from 5 to 10 minutes. If the correct axis is tipped away from the rotation axis in a plane containing the X-ray beam, the zero layer in the photograph will look like that in the top illustration of Fig. 4.7. The situation shown in the bottom illustration of Fig. 4.7 will occur if the crystal is misaligned in a plane perpendicular to the X-ray beam. The angle of misalignment (β) in each case is:

$$\text{side to side : } \tan \beta = \frac{\Delta}{r}$$

$$\text{back to front: } \tan 2\beta = \frac{\Delta}{r}$$

where r is the radius of the camera. The misalignment can be corrected using screws on the sample holder. Each time the crystal is adjusted it gets translated out of the X-ray beam, so it is necessary to go through the centering procedure after each adjustment.

Usually the misalignment is a combination of the two cases shown in Fig. 4.7. This results in a photograph that is hard to interpret, however an estimate of the back to front misalignment can still be made. Once this is corrected a second photograph will enable the side to side correction to be measured. The orientation of the crystal can be changed by 15° . Before mounting the crystal in the dewar it should be checked that the angle between the required rotation axis and the sample holder axis is within this range.

The alignment can be improved by using the counter. From the final alignment photograph one can obtain the γ coordinates of several zero layer reflections. The counter is set at the γ values and with a coarse collimator at the detector the dewar is rotated until a reflection is located. The spot is centered in the collimator by adjusting γ on either side of the spot until half the peak intensity is measured. γ is then set at the mean of these two values. The procedure is then repeated adjusting χ . The X-ray shutter is then

closed and the collimator replaced by a fine horizontal slit. The spot centering is repeated adjusting only χ and the mean value noted. Any variation in χ with γ is corrected for using the adjusting screws.

If lattice parameter measurements are to be made it is necessary that the centering of the crystal in the X-ray beam be accurate. This is best checked by measuring γ for several symmetry related zero layer reflections. A fine vertical slit should be used on the detector for this purpose, and the spots centered as before. Any variation in γ within a set can be corrected for by slight adjustments of the X and Y tables.

CHAPTER 5

REFINEMENT OF THE LOW TEMPERATURE CRYSTAL STRUCTURES OF DyAsO_4 AND TbAsO_4

Introduction

The low temperature structures of DyAsO_4 and TbAsO_4 have been refined in the orthorhombic space groups Imma and Fddd respectively. The choice of these space groups is based on evidence from powder X-ray studies (Göbel and Will 1972; Göbel 1972), and optical absorption experiments (Wappler et al 1974; Wüchner et al 1972). In the case of DyAsO_4 early powder X-ray work indicated that the low temperature cell axes, a , b and c , are related to the high temperature tetragonal axes \bar{a} and \bar{c} by

$$a = \bar{a} + \Delta$$

$$b = \bar{a} - \Delta$$

$$c = \bar{c}$$

Also it was found that the systematic absences in the low temperature phase were the same as for the high temperature phase. This fact was confirmed in the present work, using single crystals. The optical absorption spectrum of Dy^{3+} in the low temperature phase indicated that all the rare-earth ions in a unit cell are equivalent, and that their sites have point symmetry C_{2v} . These criteria leave only one choice for

the space group i.e. Imma. The atoms occupy the following positions.

Dy	4 (e)	mm	$0, \frac{1}{4}, z$
As	4 (e)	mm	$0, \frac{1}{4}, z'$
O1	8 (h)	m	$0, u, v$
O2	8 (i)	m	$u', \frac{1}{4}, v'$

The powder X-ray data for TbAsO_4 is consistent with the low temperature cell being orthorhombic with twice the volume of the tetragonal cell, or monoclinic with the same volume as the high temperature cell. Again the systematic absences are the same in both phases. The optical absorption experiments require that the rare earth ions be equivalent and have a site symmetry of D_2 . The only space group that satisfies all the above requirements is $Fddd$. The new cell axes are given by

$$a = \sqrt{2} \bar{a} + \Delta$$

$$b = \sqrt{2} \bar{a} - \Delta$$

$$c = \bar{c}$$

The atoms occupy the following positions:

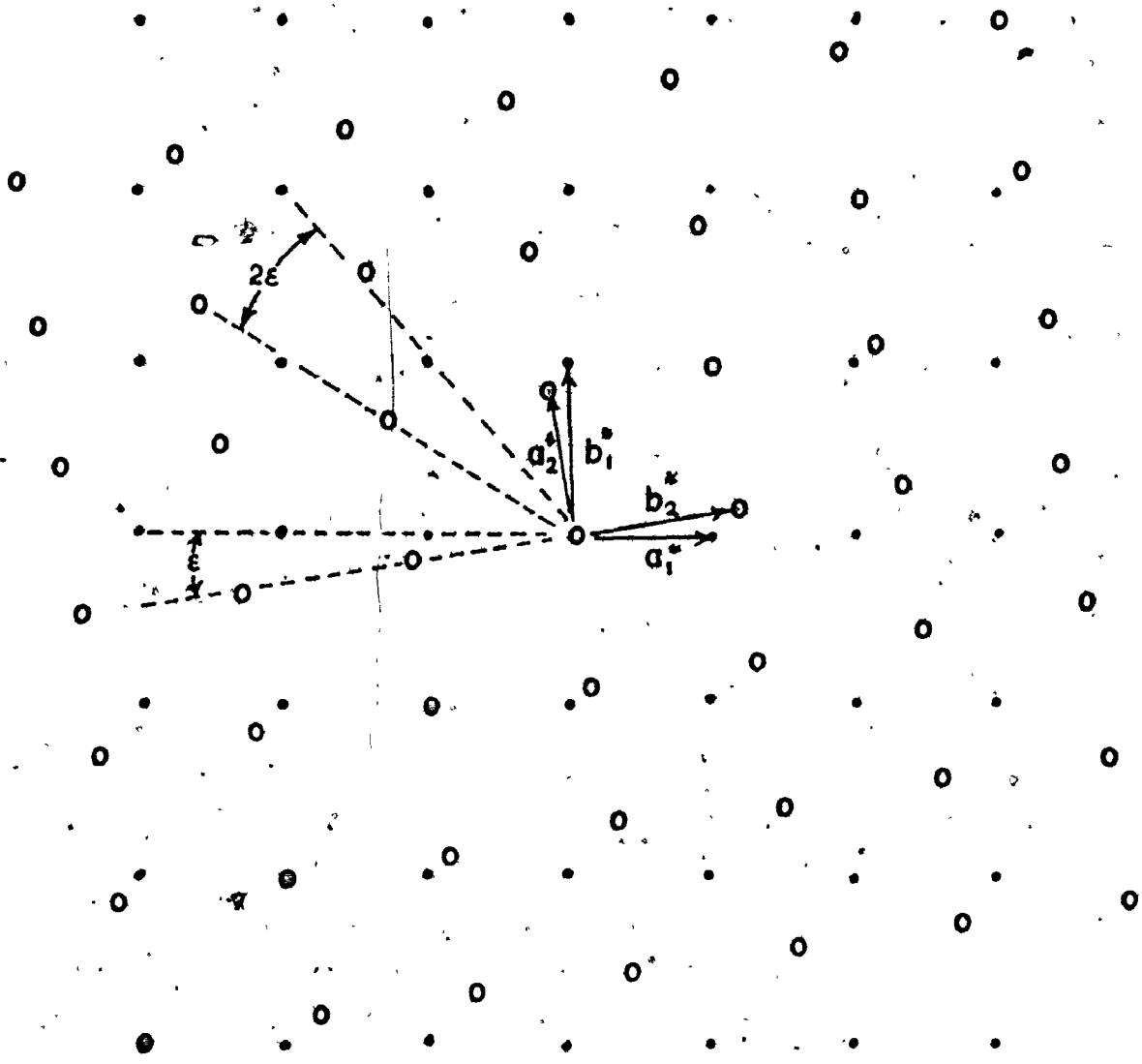
Tb:	8 (a)	222	$0, 0, 0$
As:	8 (b)	222	$0, 0, \frac{1}{2}$
O :	32 (h)	1	$u, v, w.$

Domains

The orthorhombic distortions referred to the tetragonal cell, take place along the $[1,0,0]$ directions in DyAsO_4 , and along the $[110]$ directions in TbAsO_4 . Above the transition temperature, there are two equivalent, mutually perpendicular, choices for these directions. On passing through the transition temperature different parts of the crystal have different distortion directions. This results in the crystals forming crystallographic domains. In both cases the domain boundaries are (110) planes of the orthorhombic cell (Leask et al. 1973). If all the domain boundaries are parallel the reciprocal space of the crystals will take the form shown in Fig. 5.1. Each relp, with the exception of (h,h,ℓ) relps corresponding to the domain boundary, will have two components. Usually the domain pattern consists of domains with boundaries along both the $[110]$ and $[1\bar{1}0]$ directions, resulting in a more complicated distribution of relps. However by applying a small magnetic field (≈ 0.8 kOe) along one of the distortion directions all the domains walls can be made parallel (Leask et al. 1973). The crystal can be made a single domain by the application of a large magnetic field (≈ 3 kOe). However, strains also affect the domain pattern and the method of mounting the crystals, employed in these experiments, produced strains that prevented the crystals remaining a single domain, once the field was removed. It was found that by choosing crystals with a small cross sectional area, in the basal plane,

Fig. 5.1

A reciprocal lattice plane ($l = \text{constant}$)
for a crystal consisting of two domains
whose common boundary is a (110) plane.



• DOMAIN 1

○ DOMAIN 2

samples consisting mainly (95%) of a single domain could be obtained.

The two components of each relp correspond to the two reflections (h,k,l) and (k,h,l) . Since the structures are orthorhombic it is important that the intensity measurements do not mix the two components. Care was taken during intensity measurements to only measure the intensity due to the largest domain. Reflections, for which the two components of the relp overlap, were not measured. In the case of $TbAsO_4$ the orthorhombic distortion is quite large and so the two components are well separated in reciprocal space. However for $DyAsO_4$, the separation is smaller. The intensity measurements in this case possibly contain a residual intensity due to the smaller domain. The measurements of background intensity were made on either side of both components of each relp so they would not be affected by intensity due to the small domain.

Refinement

Details of the crystals used in the structure determinations may be found in tables 5.1a and 5.1b. In each case the crystal was mounted and aligned on the low temperature diffractometer in the manner described in Chapter 4. $MoK\alpha$ radiation was used, with a zirconium β filter in the incident beam. Both crystals were aligned with their c axis along the dewar rotation axis. The lattice parameters from the powder X-ray studies were used to index reflections on the

alignment photographs. Values of γ and χ for 25 reflections with 2θ less than 40 degrees were accurately measured using the counter. These angles were then used in a least squares programme to determine a new set of cell dimensions. Using these dimensions as input a Fortran programme ROT was used to calculate the values of γ , χ and ω for reflections with 2θ less than 60 degrees.

The intensities were measured using an ω scan. With the counter set at the correct values of γ and χ the crystal was rotated to bring the reflection through the Ewald sphere. The scan rate was fixed at 7.2° per minute and the scan length was varied so that intensity due to the small domain would not be measured. The background was measured on both sides of the reflection for half the period of the scan. In terms of the scan count I_ω and the background counts I_{B1} and I_{B2} , the measured intensity is given by

$$I = I_\omega - I_{B1} - I_{B2} \quad (5.1)$$

The standard deviation in the measured intensity is

$$\sigma(I) = \sqrt{I_\omega + I_{B1} + I_{B2}} \quad (5.2)$$

Data was collected for values of l from 0 to 5 inclusive and for both negative and positive values of h and k such that 2θ was less than 60 degrees.

The measured intensities were converted to structure factors using the programme RED. This programme applied the

Lorentz polarization corrections and corrected for the absorption by the dewar. It also calculated the secondary extinction parameter $\beta(2\theta)$ and applied an absorption correction. The absorption correction was calculated using a numerical integration technique. Structure factors for symmetry related reflections were averaged.

Refinement of the structures was carried out using the least squares programme Cudls. The atomic scattering factors used were the same as those used in the room temperature studies. The initial positional parameters were set at values obtained from the room temperature structures

$$\text{i.e. DyAsO}_4 : z = 0.875 \quad , \quad z' = 0.375$$

$$u = 0.43 \quad , \quad v = 0.195$$

$$u' = 0.82 \quad , \quad v' = 0.555$$

$$\text{TbAsO}_4 : u = 0.09 \quad v = 0.09$$

$$w = 0.32 .$$

The values of z and z' , in the case of DyAsO_4 , could not be varied simultaneously since there were large correlations between these parameters. Upon varying them separately their values did not change from those given above, so they were fixed at these values for the remainder of the refinement. In the initial stages of refinement the oxygen position parameters and isotropic temperature factors for all atoms were varied, together with an overall scale constant. Once the variation of these parameters became small the temperature

factors were allowed to become anisotropic. Several cycles of refinement using anisotropic temperature factors for the oxygen atoms had no effect on the residuals and these temperature factors became non-positive definite. The remainder of the refinement was carried out using isotropic temperature factors for the oxygen atoms. In the final stages of refinement a Cruickshank weighting scheme was used, and the secondary extinction parameter was varied.

Refinement was terminated when the parameters varied by less than one-tenth of their standard deviations. The final values of the residuals are given in tables 5.1a and 5.1b. The final values of the atomic parameters are given in tables 5.2a and 5.2b and the pertinent bond distances and angles are given in tables 5.3a and 5.3b. Tables 5.4a and 5.4b list the observed and calculated structure factors.

Discussion

Since the phase transitions occur at very low temperatures, there is very little energy available, in the form of occupied phonon states, to drive the transition. Hence the difference between the two phases is slight. A discussion of the low temperature structures can conveniently be made using Fig. 3.1 and Fig. 3.2, which describe the high temperature phase.

DyAsO₄

The difference between the high and low temperature phases of DyAsO₄ can be considered as the combination of two effects. First a shift in the relative positions of the chains of molecules due to change in lattice parameters, and secondly a distortion of the AsO₄³⁻ tetrahedra.

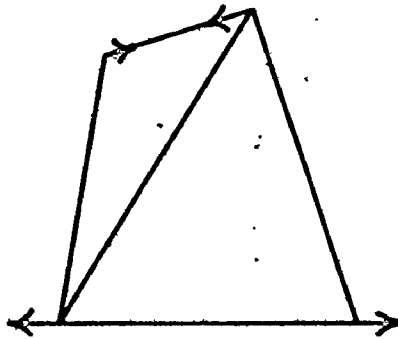
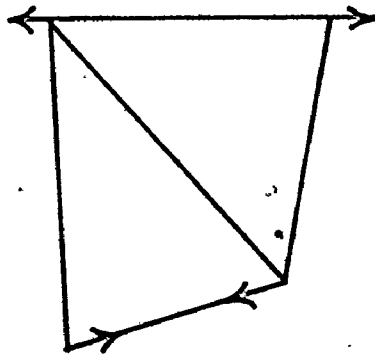
Referring to Fig. 3.1, below T_c the chains of molecules move apart along the x direction and move together along the y direction. This corresponds to a lattice strain of $e = e_{11} - e_{22}$ (Kittel, 1966) with respect to the tetragonal cell. This strain has symmetry B_{1g} and corresponds to a k=0 acoustic phonon of symmetry A_{2u}.

A discussion of the distortion of the AsO₄³⁻ tetrahedra is somewhat unreliable, based on the present data, because the errors in the bond distances and angles (Table 5.3a) are quite large. However the distortion observed does correspond to one of those expected on the basis of the theory of the phase transitions given in Chapter 6, and so a description of the distortion will be pursued.

Below the transition temperature the oxygen atoms are no longer equivalent, they are split into two groups. In terms of the AsO₄³⁻ tetrahedra the two groups correspond to the two pairs of oxygen atoms separated along the z axis. With reference to Fig. 3.2 one pair consists of those atoms labelled 5 and 6 and the other pair to those labelled 9 and 10. The distortion consists of one pair moving together along the line joining

Fig. 5.2

The mode of distortion of the AsO_4^{3-}
tetrahedra in DyAsO_4 .



them in the undistorted tetrahedra, and the other pair moving apart in a similar manner. The primitive unit cell contains two AsO_4^{3-} tetrahedra, related by a rotary inversion operation. The tetrahedra are labelled 1 and 2 in Fig. 3.1. The distortions of these two tetrahedra are shown in Fig. 5.2. Such a distortion corresponds to a $k=0$ optic phonon of symmetry B_{1g} (Dawson et al 1971) in the high temperature structure. This distortion can be considered as arising from the displacement of each of the four oxygen atoms in a tetrahedra by a distance Q . From Table 5.3a the value of Q is $1.7 \times 10^{-2} \text{ \AA}$.

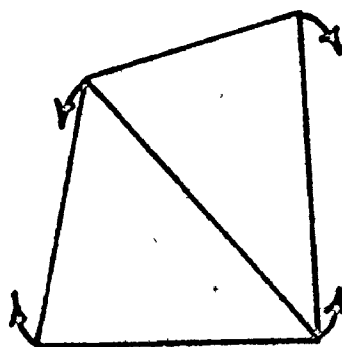
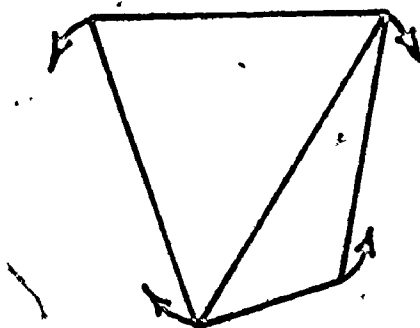
The average value of the As-O distance is 1.704 \AA . This is greater than the value of 1.676 \AA obtained at room temperature. This seems to indicate a further distortion of the tetrahedra consisting of an expansion along the As-O bonds. The expansion corresponds to a $k=0$ optic phonon of symmetry A_{1g} (Dawson et al 1971). The value of Q in this case is $2.8 \times 10^{-2} \text{ \AA}$.

TbAsO₄

In the case of TbAsO_4 the main feature of the change in structure is the shift in the relative positions of the chains of molecules due to a change in lattice parameters. With reference to Fig. 3.1 these chains move apart along the x' direction and together along the y' direction. This corresponds to a lattice strain of $e = e_{xy}$, with respect to the high temperature structure. This strain has symmetry B_{2g} and corres-

Fig. 5.3

The mode of distortion of the AsO_4^{3-}
tetrahedra in TbAsO_4 .



ponds to the $k=0$ acoustic phonon A_{1u} .

There also appears to be evidence of a distortion of the AsO_4^{3-} tetrahedra as shown in Fig. 5.3. This distortion corresponds to a $k=0$ optical phonon of symmetry A_{1g} (Dawson et al 1971) in the space group $I4_1/amd$. The value of Q for this phonon mode is $5.3 \times 10^{-2} \text{ \AA}$.

Table 5.1a

Crystal data for DyAsO₄ at 6°K

Lattice parameters: $a = 7.056(5)\text{Å}$; $b = 7.026(5)\text{Å}$;
 $c = 6.297(6)\text{Å}$; $\alpha = \beta = \gamma = 90^\circ$

Faces bounding the crystal and the distance (d) along the face normal to a point inside the crystal	<u>Crystal face</u>	<u>d mm.</u>
	(1,1,0)	.050(8)
	($\bar{1}$,0,0)	.050(8)
	(0,1,0)	.050(8)
	(0, $\bar{1}$,0)	.050(8)
	(0,0,1)	.247(8)
	(0,0, $\bar{1}$)	.247(8)

Linear absorption coefficient: $\mu = 352.9 \text{ cm}^{-1}$

Total number of reflections measured: 415

Number of unique reflections: 105

Weighting function: $\frac{1}{w} = 195.1 - 0.388|F_0| + 0.0012|F_0|^2 + 1665 \frac{\sigma(F_0)^2}{|F_0|}$

Secondary extinction parameter: $g = 5.51 \times 10^{-7}$

Final residuals: $R_w = 0.058$; $R = 0.055$

Table 5.1b

Crystal data for TbAsO₄ at 6°K

Lattice parameters: $a = 10.120(5)\overset{\circ}{\text{Å}}$; $b = 9.945(5)\overset{\circ}{\text{Å}}$;
 $c = 6.310(6)\overset{\circ}{\text{Å}}$; $\alpha = \beta = \gamma = 90^\circ$

Faces bounding the crystal and the distance (d) along the face normal to a point inside the crystal	<u>Crystal face</u>	<u>d mm.</u>
	(1,1,0)	.067(8)
	($\bar{1},\bar{1},0$)	.067(8)
	($\bar{1},1,0$)	.083(8)
	(1, $\bar{1},0$)	.083(8)
	(0,0,1)	.283(8)
	(0,0, $\bar{1}$)	.283(8)

Linear absorption coefficient: $\mu = 304.8 \text{ cm}^{-1}$

Total number of reflections measured: 243

Number of unique reflections: 83

Weighting function: $\frac{1}{w} = 20.77 - 0.088|F_0| + 0.0001|F_0|^2 + 100.0 \frac{\sigma(F_0)^2}{|F_0|}$

Secondary extinction parameter: $g = 1.09 \times 10^{-6}$

Final residuals: $R_w = 0.019$; $R = 0.019$

Table 5.2a

Final atomic parameters for DyAsO₄ at 6°K

Atom	x	y	z	U _{iso}	U ₁₁	U ₂₂	U ₃₃
Dy	0.0	0.25	0.875	-	77(17)	69(18)	59(25)
As	0.0	0.25	0.375	-	76(23)	65(26)	9(40)
O1	0.0	0.434(4)	0.201(4)	154(64)			
O2	0.812(5)	0.25	0.547(5)	285(78)			

Table 5.2b

Final atomic parameters for TbAsO₄ at 6°K

Atom	x	y	z	U _{iso}	U ₁₁	U ₂₂	U ₃₃
Tb	0.0	0.0	0.0	-	9(9)	7(9)	1(12)
As	0.0	0.0	0.5	-	28(12)	11(12)	2(18)
O	0.090(1)	0.092(1)	0.331(2)	78(21)			

Table 5.3a
Bond lengths and angles for DyAsO₄ at 6°K

Atoms	Distance Å	Atoms	Angles (°)
As-01	1.692 (28)	02 (1) *-Dy-02 (2)	155.0 (1.2)
As-02	1.715 (33)	01 (3) -Dy-01 (4)	155.6 (9)
Dy-02 (1)	2.255 (32)	02 (1) -Dy-01 (3)	92.6 (2)
Dy-01 (3)	2.273 (28)	01 (5) -Dy-01 (6)	64.3 (9)
Dy-01 (5)	2.428 (27)	02 (9) -Dy-02 (10)	65.5 (1.1)
Dy-02 (8)	2.452 (34)	01 (5) -Dy-02 (7)	135.4 (7)
01 (5) -01 (6)	2.584 (40)	01 (5) -As-01 (6)	99.5 (1.3)
02 (7) -02 (8)	2.653 (46)	02 (9) -As-02 (10)	101.4 (1.6)
01 (3) -01 (5)	2.702 (38)	01 (5) -As-02 (9)	114.2 (8)
01 (5) -02 (9)	2.860 (39)		
02 (1) -01 (5)	2.995 (35)		
02 (1) -01 (3)	3.274 (32)		

*The label on the oxygen atoms refers to Fig. 3.2.

Table 5.3b

Bond lengths and angles for TbAsO₄ at 6°K

Atoms	Distance Å	Atoms	Angles (°)
As-0	1.677(11)	0(1)-Tb-0(2)	154.5(4)
Tb-0(1)	2.311(10)	0(2)-Tb-0(3)	91.2(3)
Tb-0(5)	2.456(11)	0(5)-Tb-0(6)	63.6(3)
0(5)-0(6)	2.587(13)	0(5)-Tb-0(7)	136.2(3)
0(3)-0(5)	2.770(17)	0(5)-As-0(6)	100.9(5)
0(5)-0(9)	2.813(16)	0(5)-As-0(9)	114.0(5)
0(1)-0(5)	3.027(15)		
0(1)-0(3)	3.302(15)		

CHAPTER 6

THEORY OF THE PHASE TRANSITION IN THE RARE EARTH ARSENATES AND VANADATES

Introduction

The key to understanding the second order crystallographic phase transitions in these compounds is the fact that the crystal field favours a large quadrupole moment in the basal plane. This fact coupled with the four fold symmetry about the c axis (above T_c) results in near degeneracies of the four lowest lying electronic states. Below T_c these degeneracies are lifted, as shown in Fig. 6.1. In the low temperature phase the quadrupoles lie along a particular direction, above T_c half lie along this direction and half along an axis orthogonal to the first. Hence the transition may be regarded as 'ferroquadrupolar'. The effective quadrupole coupling has been the subject of much study. A recent review article by Gehring and Gehring (1975) provides an excellent set of references for earlier works. The greatest success has been obtained with a theory invoking a cooperative Jahn-Teller coupling between the rare earth ions. The coupling mechanism involves lattice distortion (Elliot et al 1972). The rest of this chapter will be concerned with an outline of this theory.

The Jahn-Teller Theorem

This theorem states that any complex, other than a linear molecule, occupying a state with electronic orbital degeneracy, when the nuclei are in a symmetric configuration, is unstable with respect to at least one asymmetric distortion that removes the degeneracy in first order. The instability arises because the centre of gravity of the degenerate level remains unchanged (Sturge, 1967), so a linear splitting necessarily leads to a level of lower energy than the unsplit level. Jahn and Teller (1937) proved that such a distortion is available from an examination of the point symmetry group in all possible cases.

The Jahn-Teller theorem is a special case of a much broader class of effects due to the breakdown of the Born-Oppenheimer approximation (Sturge, 1967). In this approximation the motion of the electrons in the unfilled shells of ions is independent of the nuclear motion. This assumes that the electronic motion is so rapid compared with that of the nuclei, that the electrons see a potential which only depends parametrically on the nuclear coordinates. This may be restated as, the energies of the lattice excitations (phonons) must be lower than the energies of electronic excitations. Clearly this is not the case when there are electronic orbital degeneracies, resulting in a large coupling between electronic states and lattice distortions. There will also be this type of coupling for non-degenerate electronic states as long as their

separation is small compared with the energies of phonons. The latter is the case for the rare earth compounds considered here. Their almost degenerate ground state quartet is well separated, approximately 100 cm^{-1} , from other levels, so only these four levels will be of importance in the coupling to lattice distortions.

If the point group of the complex is G the displacements of the nuclei can be written in terms of $Q_{\Gamma\alpha}$. These are linear combinations of the displacement of individual nuclei that transform according to the α component of the Γ irreducible representation of G . If the degenerate energy levels transform as the $\bar{\Gamma}$ irreducible representation of G , then the only distortions that can remove the degeneracy must transform according to one of the irreducible representations of G contained in the direct product $\Gamma \times \bar{\Gamma}$. For the rare earth arsenates and vanadates the point group symmetry at the rare earth site is D_{2d} . The representations that the lowest four levels belong to are given in Fig. 6.1. By examining the relevant direct products one finds that the only distortions, that can remove the near degeneracies, belong to the representations A_1 , B_1 , B_2 and E . The mode chosen will be the one with the largest coupling.

Electron States

In the case of Dy^{3+} , below T_c the lowest electronic doublet has the spectroscopic splitting factors $g_x = g$.

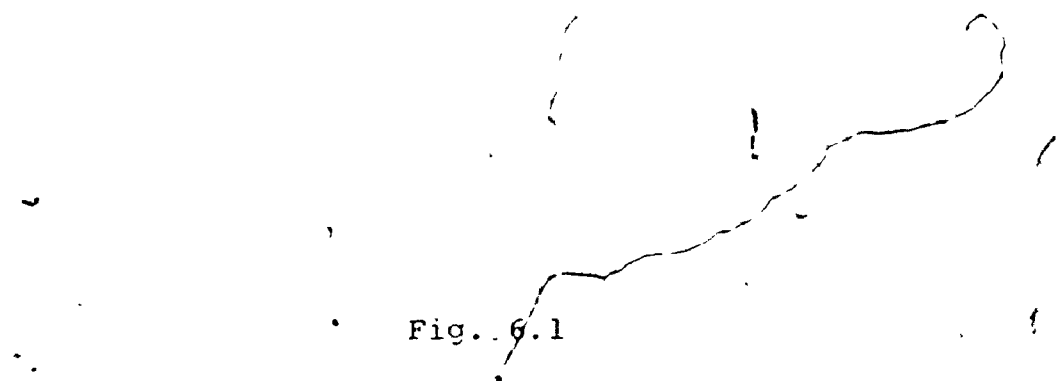
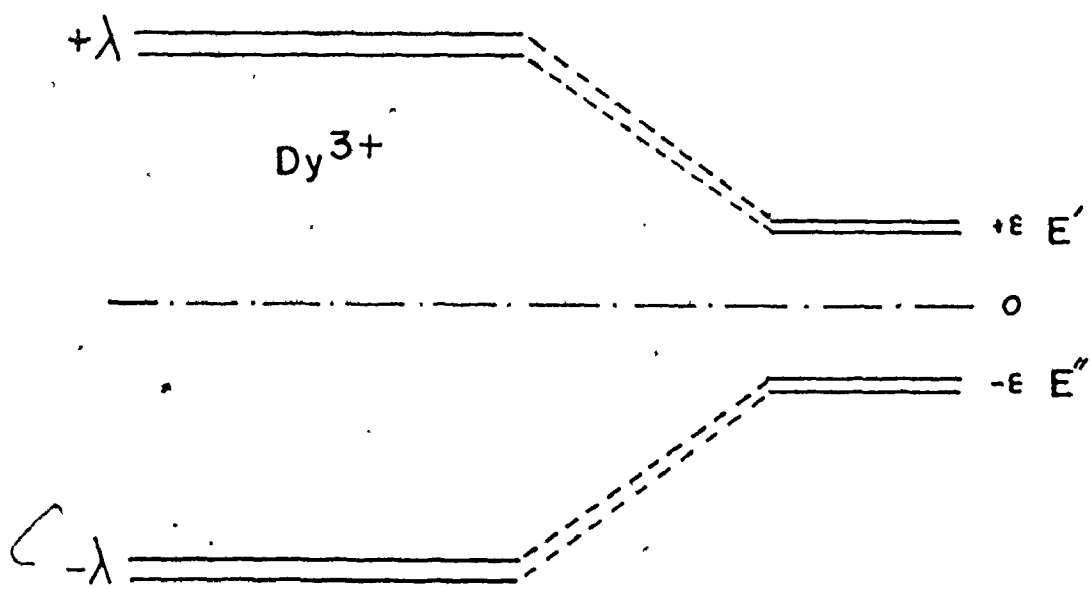
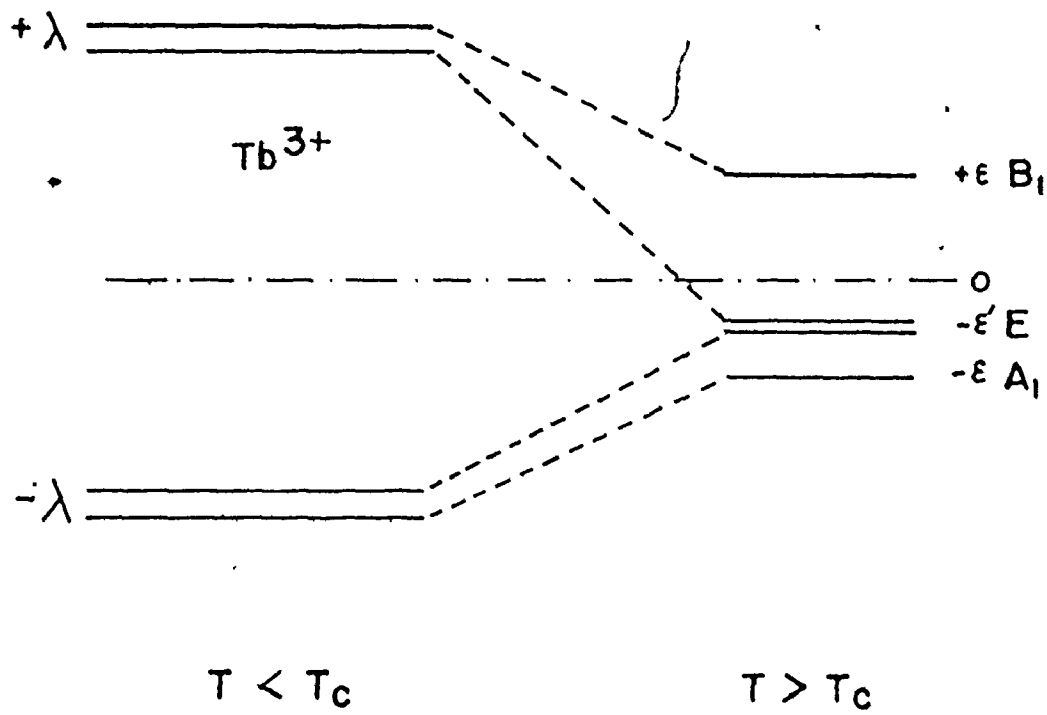


Fig. 6.1

The lowest electronic states of Dy^{3+} and Tb^{3+} above and below the Jahn-Teller transition temperature.

The upper case letters are the group theory designations and the lower case ϵ 's are the energies.



$g_y = 0$ and $g_z = 0$ (Ellis et al 1971; Wright and Moos 1971). The excited doublet has $g_x = 0$, $g_y = g$ and $g_z = 0$. For both DyVO_4 and DyAsO_4 g has a value close to 20, the maximum allowable g value for the $J = 15/2$ ground term of Dy^{3+} (${}^6\text{H}_{15/2}$). Thus the two doublets correspond to the states $|J_x = \pm J\rangle$ and $|J_y = \pm J\rangle$ (Klein et al 1971).

A similar situation occurs for Tb^{3+} except that the maximum g value occurs in the directions x' and y' which are at 45° to x and y in the basal plane. The low temperature doublets correspond to the states $|J_{x'} = \pm J\rangle$ and $|J_{y'} = \pm J\rangle$. The ground terms of the terbium ion is ${}^7\text{F}_6$.

The pairs of states forming the low temperature doublets have charge clouds in the shape of flat pancakes that intersect along the z axis. These correspond approximately to electric (magnetic) quadrupoles. As stated before, the phase transition can be regarded as the lowering of the energy of one possible quadrupole orientation relative to the other (Gehring and Gehring 1975).

The high temperature states are the appropriate linear combinations of the low temperature states that transform according to the correct irreducible representation of D_{2d} (Elliot et al 1972).

Single Ion-lattice Coupling

The interaction between the electronic states and distortions of the ions surrounding the rare earth site may be written as

$$H_s = \sum_{\Gamma\alpha} B_{\Gamma} Q_{\Gamma\alpha} O_{\Gamma\alpha} \quad (6.1)$$

where the summation runs over all those irreducible representations of D_{2d} that can cause a lifting of the degeneracies. The B_{Γ} 's are coupling coefficients and $O_{\Gamma\alpha}$ is an electronic operator of the same family of operators used in writing the crystal field Hamiltonian.

Elliot et al (1972) have evaluated the interaction matrix for both Dy^{3+} and Tb^{3+} . It is found that in each case there is only one dominant mode of distortion. For Dy^{3+} this is the B_2 mode and for Tb^{3+} it is the B_1 mode. These correspond to the even, parity $k=0$ lattice modes B_{1g} and B_{2g} respectively. Throughout the remainder of this chapter only coupling to these modes will be considered. Elliot et al (1972) represent the operators $O_{\Gamma\alpha}$ by six 4×4 unitary matrices σ^i and τ^i . This has the advantage that the terms in σ^z produce the distortion. The σ matrices produce splittings between the low temperature doublets and the τ matrices distinguish between the levels of the doublets. If terms in which τ appears are neglected, i.e. the doublets are treated as singlets, then the σ matrices become the Pauli spin matrices. In terms of these new matrices and new coupling coefficients (S_{Γ}) the interaction Hamiltonian becomes

$$H_s^{Dy^{3+}} = S_{B2} Q_{B2} \sigma^z, \quad (6.2)$$

$$H_s^{Tb^{3+}} = S_{B1} Q_{B1} \sigma^z. \quad (6.3)$$

Crystal field

The crystal field splitting of the four lowest levels of the rare earth ions, has so far been ignored. These splittings have important effects on the phase transitions, so they must be included in the final Hamiltonian. The inclusion of the crystal field effects is easily done in terms of the σ and τ matrices. Elliot et al (1972) have shown that

$$H_c^{Dy^{3+}} = -\epsilon \sigma^x, \quad (6.4)$$

$$H_c^{Tb^{3+}} = -\frac{1}{2} \epsilon (1 + \tau^2) \sigma^x \quad (6.5)$$

where ϵ refers to the splittings indicated in Fig. 6.1. In the case of Tb^{3+} ϵ' has been set to zero but will be included later.

Electron-phonon Coupling

The displacements of the ions surrounding each rare earth site are coupled to those around neighbouring sites by the lattice phonons. The vibrational part of the Hamiltonian may be written

$$H_p = \sum_{n, \underline{k}} \hbar \omega_n(\underline{k}) \left[C_n^+(\underline{k}) C_n(\underline{k}) + \frac{1}{2} \right]. \quad (6.6)$$

$C_n^+(\underline{k})$, $C_n(\underline{k})$ are the usual phonon creation and annihilation operators, n is the branch index and \underline{k} is the wave vector.

If we use ρ to label the two rare earth sites in the ℓ^{th} primitive cell centred at $R(\ell)$ we may define new electronic operators

$$\sigma^{\Gamma}(\rho, \underline{k}) = \frac{1}{\sqrt{N}} \sum_{\ell} \sigma^{\Gamma}(\rho, \ell) e^{-i \underline{k} \cdot \underline{R}(\ell)} \quad (6.7)$$

The lattice displacement of symmetry Γ produced by the phonon (n, \underline{k}) is given by

$$Q_{\Gamma} = T_{\Gamma}(n, \underline{k}) [C_n^{\Gamma}(\underline{k}) + C_n(\underline{k})] (\hbar/2\mu\omega_n(\underline{k}))^{1/2} \quad (6.8)$$

here $T_{\Gamma}(n, \underline{k})$ is the projection of the phonon Q_{Γ} and μ is the effective mass of the cage of surrounding ions. Similarly the coupling to the phonon (n, \underline{k}) can be described by $R_n^{\Gamma}(\rho, \underline{k})$ where

$$S_{\Gamma} = \frac{R_n^{\Gamma}(\rho, \underline{k})}{T_{\Gamma}(n, \underline{k})} (\hbar/2\mu\omega_n(\underline{k}))^{-1/2} \quad (6.9)$$

We may now write the interaction Hamiltonian as

$$H_S^{\Gamma} = \sum_{n, \underline{k}, \rho} R_n^{\Gamma}(\rho, \underline{k}) [C_n^{\Gamma}(-\underline{k}) + C_n(\underline{k})] \sigma^{\Gamma}(\rho, \underline{k}), \quad (6.10)$$

where Γ refers to B_2 in the Dy^{3+} case and B_1 in the Tb^{3+} case.

Since the main interest is in the $k=0$ modes the dependence on ρ may be neglected (Elliot et al 1972). The displaced phonon operators are defined as

$$\begin{aligned} Y_n^{\Gamma}(\underline{k}) &= [C_n^{\Gamma}(\underline{k}) + \frac{R_n^{\Gamma}(\underline{k})}{\hbar\omega_n(\underline{k})} \sigma_n^{\Gamma}(\underline{k})] \\ Y_n(\underline{k}) &= [C_n(\underline{k}) + \frac{R_n(\underline{k})}{\hbar\omega_n(\underline{k})} \sigma_n^{\Gamma}(\underline{k})] \end{aligned} \quad (6.11)$$

The physical meaning of these operators is that they describe lattice excitations relative to the distortion, whereas the $C_n(\underline{k})$ describe excitations with respect to the undistorted

phase. The total Hamiltonian $H = H_p + H_c + H_s$ may then be written.

$$H^{Dy^{3+}} = \sum_{\tilde{k}, n} \hbar \omega_n(\tilde{k}) (\gamma_n^+(\tilde{k}) \gamma_n(\tilde{k}) + \frac{1}{2}) - \frac{1}{2} \sum_{\substack{\ell, \ell' \\ \ell \neq \ell'}} J(\ell, \ell') \sigma^z(\ell) \sigma^z(\ell') - \sum_{\ell} \epsilon \sigma^x(\ell), \quad (6.12)$$

$$H^{Tb^{3+}} = \sum_{\tilde{k}, n} \hbar \omega_n(\tilde{k}) (\gamma_n^+(\tilde{k}) \gamma_n(\tilde{k}) + \frac{1}{2}) - \frac{1}{2} \sum_{\substack{\ell, \ell' \\ \ell \neq \ell'}} J(\ell, \ell') \sigma^z(\ell) \sigma^z(\ell') - \frac{1}{2} \sum_{\ell} \epsilon (1 + \tau^2) \sigma^x(\ell) \quad (6.13)$$

where

$$J(\ell, \ell') = \frac{1}{N} \sum_{n, \tilde{k}} \frac{R_n^{\Gamma}(\tilde{k})^2}{\hbar \omega_n(\tilde{k})} \exp(i\tilde{k} \cdot [R(\ell) - R(\ell')]) \quad (6.14)$$

The terms with $\ell = \ell'$ have been subtracted from equations (6.12) and (6.13) since they do not assist the ordering. They represent the Jahn-Teller self energy of a single complex, hence they only shift the zero of energy.

Molecular Field Theory

If we ignore the residual crystal field splittings the order predicted by equations (6.12) and (6.13) is that of the Ising model of magnetism. It predicts a cooperative transition for the maximum value of

$$J(\tilde{k}) = \sum_n K_n(\tilde{k}) - \frac{1}{N} \sum_{n, \tilde{q}} K_n(\tilde{q}) \quad (6.15)$$

where

$$K_n(\underline{k}) = \frac{R_n^\Gamma(\underline{k})}{\omega_n(\underline{k})} \quad (6.16)$$

Later on we shall be assuming that this maximum value occurs for $k=0$. Periodic boundary conditions exclude bulk deformations of the lattice by $k=0$ acoustic phonons. Therefore $K_a(0) = 0$ and all $k=0$ acoustic modes must be dealt with separately. The contributions to $J(\underline{k})$ can be split up into an optic mode component $J_0(\underline{k})$ and an acoustic contribution

$\sum_{n=a} K_n(\underline{k}) - v$ where

$$v = \frac{1}{N} \sum_{n=a} \sum_{\underline{k}} K_n(\underline{k}) \quad (6.17)$$

then

$$J(\underline{k}) = J_0(\underline{k}) + \sum_{n=a} K_n(\underline{k}) - v \quad (6.18)$$

Elliot et al (1972) state that the optic mode coupling is expected to be short range. If we assume that there is only coupling to z nearest neighbours, then in the limit of small k $J_0(\underline{k})$ tends to a constant (Gehring and Gehring 1975)

$$\lim_{k \rightarrow 0} J_0(\underline{k}) = zj \quad (6.19)$$

In the molecular field approximation the transition occurs, when $J(\underline{k})$ has its maximum value $J(0)$, at T_c given by

$$k_B T_c = J(0) = \sum_{\ell, \ell'} J(\ell, \ell') \quad (6.20)$$

The order parameter for the transition is $\langle \sigma^z(\ell) \rangle$, and the "pseudo-spin" states $|\sigma^z(\ell)\rangle$ are split by $\pm J(0) \langle \sigma^z(\ell) \rangle$. The

two spin states correspond to different orientations of the quadrupole moments. $|\sigma^z(\ell)=+1\rangle$ represents the state with the quadrupole aligned along the $x(x')$ axis and $|\sigma^z(\ell)=-1\rangle$ is the state with the quadrupoles aligned along the $y(y')$ axis.

The inclusion of the crystal field term makes the Hamiltonian that of the Ising model in a transverse field. The eigenvalues in this case are

$$Dy^{3+} : \pm W = ([J(0)\langle\sigma^z\rangle]^2 + \epsilon^2)^{1/2}, \quad (6.21)$$

$$\begin{aligned} Tb^{3+} : \pm W_1 &= ([J(0)\langle\sigma^z\rangle]^2 + \epsilon^2)^{1/2} \\ \pm W_2 &= J(0)\langle\sigma^z\rangle. \end{aligned} \quad (6.22)$$

Strain Coupling

Again due to the periodic boundary conditions we must consider coupling to strain separately. The strain coupling parameter represents the acoustic mode coupling in the mode in which the lattice distortion actually takes place.

The macroscopic strains associated with the transitions have the same symmetry as the dominant phonon modes i.e.

$$Dy^{3+} : e = e_{B_{1g}} = e_{xx} - e_{yy}, \quad (6.23)$$

$$Tb^{3+} : e = e_{B_{2g}} = e_{x'x'} - e_{y'y'}. \quad (6.24)$$

Hence the rare earth ions couple to the strain through a term

$$-\eta_{\Gamma} e_{\Gamma} \sigma^z. \quad (6.25)$$

The interaction Hamiltonians are then given by

$$H_S^{EY^{3+}} = -\epsilon \sigma^x - (J(0) \langle \sigma^z \rangle + \eta e) \sigma^z, \quad (6.26)$$

$$H_S^{Tb^{3+}} = -\frac{1}{2}(1+\tau^2) \sigma^x - (J(0) \langle \sigma^z \rangle + \eta e) \sigma^z. \quad (6.27)$$

The eigenvalues become

$$Dy^{3+} : \pm W = (J(0) \langle \sigma^z \rangle + \eta e)^2 + \epsilon^2)^{1/2}, \quad (6.28)$$

$$Tb^{3+} : \pm W_1 = (J(0) \langle \sigma^z \rangle + \eta e)^2 + \epsilon^2)^{1/2} \quad (6.29)$$

$$\pm W_2 = J(0) \langle \sigma^z \rangle + \eta e$$

The equilibrium value of the strain $\langle e \rangle$ can be found using the condition of mechanical equilibrium i.e. zero stress.

This leads to

$$Dy^{3+} : \langle e \rangle = \frac{\epsilon}{V_0 (C_{11} - C_{12})}, \quad (6.30)$$

$$Tb^{3+} : \langle e \rangle = \frac{2\eta \langle \sigma^z \rangle}{V_0 C_{66}}. \quad (6.31)$$

V_0 is the volume of the primitive unit cell and C_{11} , C_{12} and C_{66} are the usual elastic constants of the tetragonal phase in the absence of a transition. The molecular field parameter then becomes $\lambda = J(0) + \mu$, where μ is given by

$$Dy^{3+} : \mu = \frac{4\eta^2}{V_0 (C_{11} - C_{12})}, \quad (6.32)$$

$$Tb^{3+} : \mu = \frac{2\eta^2}{V_0 C_{66}}. \quad (6.33)$$

The equilibrium value of the order parameter $\langle \sigma^z \rangle$ can be

found by minimizing the Helmholtz free energy. This gives

$$\text{Dy}^{3+} : \langle \sigma^z \rangle = \frac{\lambda \langle \sigma^z \rangle}{W} \tanh\left(\frac{W}{k_B T}\right), \quad (6.34)$$

$$\text{Tb}^{3+} : \langle \sigma^z \rangle = \left[\frac{\lambda \langle \sigma^z \rangle}{W_1} \sinh\left(\frac{W_1}{k_B T}\right) + \exp\left(\frac{-\epsilon'}{k_B T}\right) \sinh\left(\frac{W_2}{k_B T}\right) \right] \quad (6.35)$$

$$\left[\cosh\left(\frac{W_1}{k_B T}\right) + \exp\left(\frac{-\epsilon'}{k_B T}\right) \cosh\left(\frac{W_2}{k_B T}\right) \right]^{-1}$$

In the expression for Tb^{3+} the terms including the crystal field parameter ϵ' have been reintroduced. The transition temperatures can be obtained from equations (6.34) and (6.35) in the limit of $\langle \sigma^z \rangle \rightarrow 0$

$$\text{Dy}^{3+} : \epsilon = \lambda \tanh\left(\frac{\epsilon}{k_B T_C}\right) \quad (6.36)$$

$$\text{Tb}^{3+} : \cosh\left(\frac{\epsilon}{k_B T_C}\right) + \exp\left(\frac{-\epsilon'}{k_B T_C}\right) = \frac{\lambda}{\epsilon} \sinh\left(\frac{\epsilon}{k_B T_C}\right) + \frac{\lambda}{k_B T_C} \exp\left(\frac{-\epsilon'}{k_B T_C}\right). \quad (6.37)$$

The mean field approximation is only valid if the interaction is of long range, i.e. $J_0(0)$ must be small. How well the theory works in the various cases can be seen in Table 6.1. Here the parameters λ , ϵ , ϵ' and T_C , as measured by optical spectroscopy, are given together with the value of T_C calculated using equations (6.36) and (6.37). We note that for the terbium compounds the mean field theory works well. However in the case of the dysprosium compounds the theory predicts a value of T_C that is too high. This suggests that for the terbium compounds the quadrupole coupling is long

range and for the dysprosium compounds it is of short range. This fact is confirmed by Harley and Macfarlane (1975) who measured the critical exponent β for DyVO_4 and TbVO_4 , obtaining values of 0.34 and 0.50 respectively.

To account for the behaviour of the dysprosium compounds it is necessary to make modification to the mean field theory which take account of the short range nature of the interactions. For short range interactions the mean field at a pseudo-spin site will fluctuate due to the fluctuations of the surrounding spins. Gehring et al (1972) have attempted to include the effects of short range order by accounting for these fluctuations. They replace the mean field at a site ℓ by

$$\sum_{\ell' \neq \ell} \langle \sigma_{\ell'}^z \rangle + \delta_{\ell} \quad (6.38)$$

where

$$\langle \delta_{\ell} \rangle = 0 \quad (6.39)$$

and

$$\langle \delta_{\ell}^2 \rangle = 1 - \langle \sigma_{\ell}^z \rangle^2 \quad (6.40)$$

In the absence of a crystal field splitting the mean field Hamiltonian takes the form

$$H_s = -\frac{1}{2} \sum_{\substack{\ell, \ell' \\ \ell \neq \ell'}} J(\ell, \ell') (\langle \sigma_{\ell}^z \rangle + \delta_{\ell}) \sigma_{\ell'}^z \quad (6.41)$$

Gehring et al obtain an expression for $\langle \sigma_{\ell}^z \rangle$ and expand it to second order in δ_{ℓ} . Including the crystal field term in the Hamiltonian they obtain

Table 6.1

Comparison of observed and calculated transition temperatures for the rare earth arsenates and vanadates

Compound	λ cm ⁻¹	ν cm ⁻¹	ϵ' cm ⁻¹	T_c (calculated) K	T_c (measured) K
DyVO ₄	13.8 ¹	4.5 ¹	-	18.5	14.0 ¹
DyAsO ₄	12.5 ²	3.05 ²	-	17.8	11.2 ²
TbVO ₄	25.6 ³	9.0 ³	0.0 ³	36.0	34.0 ³
TbAsO ₄	20.0 ⁴	7.65 ⁴	-1.85 ⁴	28.0	27.7 ⁴

¹Gehring et al 1971

²Wappler 1974

³Elliot et al 1972

⁴Klein et al 1971

82

$$\langle \sigma_{\ell}^z \rangle = L_0 \left[\frac{1}{2\Gamma} \frac{(1-L_0^2)}{1-Q} \frac{\epsilon^2}{\lambda^2 \langle \sigma_{\ell}^z \rangle^3} \left(1 - L_0 \lambda \frac{(3\lambda^2 \langle \sigma_{\ell}^z \rangle^2 - 2\epsilon^2)}{\lambda^3 \langle \sigma_{\ell}^z \rangle^3} \right) + \frac{L_0 (1-L_0^2)^2}{\Gamma(1-Q)} \left(\frac{\lambda^2 \langle \sigma_{\ell}^z \rangle^2 - \epsilon^2}{\lambda^2 \langle \sigma_{\ell}^z \rangle^2} \right) \left(\frac{\lambda}{k_B T} \right)^2 \right] \quad (6.42)$$

where

$$\Gamma = \frac{[\sum_{\ell} J(\ell, \ell')]^2}{\sum_{\ell} (J(\ell, \ell'))^2} \quad (6.43)$$

$$Q = \frac{1}{\Gamma} L_0^2 \left(\frac{\lambda}{\lambda \langle \sigma_{\ell}^z \rangle} \right)^2 \left(\frac{\epsilon}{\lambda \langle \sigma_{\ell}^z \rangle} \right)^4 \quad (6.44)$$

and

$$L_0 = \frac{\lambda \langle \sigma_{\ell}^z \rangle}{W} \tanh\left(\frac{W}{k_B T}\right) \quad (6.45)$$

If it is assumed that the coupling $J(\ell, \ell')$ is isotropic with magnitude j , and that it extends over z neighbours, then

$$\Gamma = \frac{(jz)^2}{zj^2} = z \quad (6.46)$$

Thus Γ can be interpreted as the number of nearest neighbours, which is 4 for the zircon structure.

CHAPTER 7

THE JAHN-TELLER TRANSITION IN DyAsO_4 and TbAsO_4

In this chapter the details of the phase transitions in these two compounds will be compared with the theory developed in Chapter 6. This comparison with theory will involve the changes in structure, discussed in Chapter 5, and the temperature dependence of the order parameter. This last quantity is easily measured using the low temperature diffractometer. The order parameter is directly proportional to the lattice strain.

Measurement of the Order Parameter

The existence of two domains in a sample results in a reciprocal space as shown in Fig. 5.1. For reflections of the type (h, h, ℓ) the angle between the two components of the relp is 2ϵ where

$$\tan \epsilon = \frac{a-b}{a_0} \quad (7.1)$$

$$(a_0 = \frac{a+b}{2})$$

Thus measuring the angle 2ϵ gives the lattice strain. The angle was measured using the (220) reflections. The detector was set at the correct angle γ and the dewar rotated through both components of the relp. The output of the rate meter was connected to a strip chart recorder. From the recorder trace ϵ

could be determined. This measurement was repeated at several temperatures below the transition temperature. Very close to T_c the traces become hard to interpret because the two peaks overlap. The smallest strain that could be measured confidently in this manner was approximately 10^{-3} .

Temperature Dependence of the Order Parameter for DyAsO₄

The measured temperature dependence of the lattice strain, i.e. the order parameter, is shown in Fig. 7.1. It was noted in Chapter 6 that molecular field theory does not give an adequate description of the phase transition in DyAsO₄. The result of a molecular field calculation (Equations (6.30) and (6.34)) is shown as the full curve in Fig. 7.1. The parameters used in this calculation are those given in Table 6.1. The value of η was chosen to give a strain of 4.7×10^{-3} at $T = 0^\circ\text{K}$. Values of the elastic constants C_{11} and C_{22} are not available for DyAsO₄. The values for TbVO₄ and DyVO₄ (Sandercock et al 1972) are almost the same and so one might expect similar values for DyAsO₄. The values used in the molecular field calculation were those for DyVO₄, i.e. $C_{11} - C_{22} = 21.6 \times 10^{11}$ dyne/cm².

Also shown in Fig. 7.1 (dotted curve) is the result of a short range order calculation using equation (6.42) and equation (6.30). The value of the parameter λ was adjusted to give the observed value of the transition temperature, which was 10°K . This yielded a value of 9.8 cm^{-1} for λ . The value of Γ was chosen as 4, and η was chosen to give a strain of

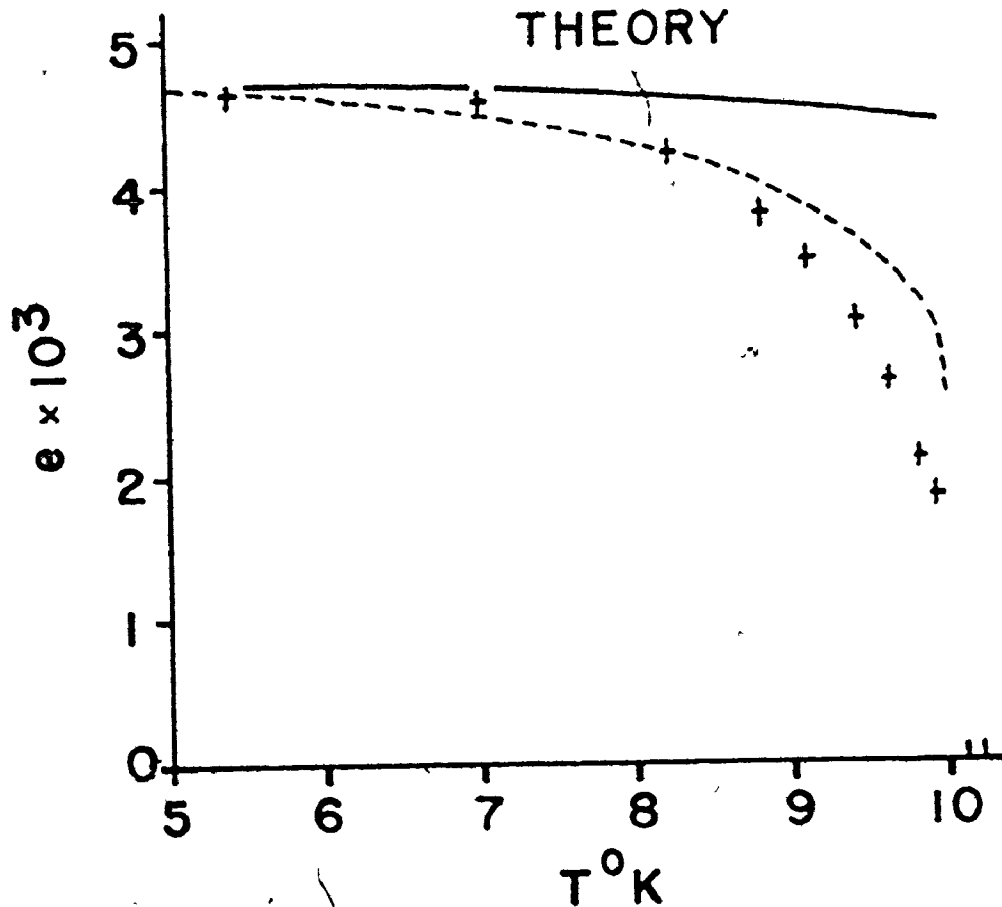
Fig. 7.1

Temperature dependence of the order parameter
(strain) for DyAsO_4 .



DyAsO₄

— MEAN FIELD THEORY
--- MODIFIED MEAN FIELD THEORY



$4.7 \cdot 10^{-3}$ at $T = 0^\circ\text{K}$. The remainder of the parameters have the same value as for the molecular field calculation. It is clear that a much better agreement is obtained if the short range nature of the interaction is taken into account. From the value of η chosen, the value of the strain coupling parameter μ can be observed from equation (6.32). This gives

$$\mu = 10.37 \text{ cm}^{-1}. \quad (7.2)$$

This is close to the value of 9.7 cm^{-1} obtained for DyVO_4 (Sandercock et al 1972). Because of the similarities of these two systems similar values are expected for the coupling coefficients. Using equation (6.18) an estimate can be made of the values of the optic mode and acoustic mode coupling coefficients, j and ν . For coupling to $k=0$ phonon modes

$$\lambda = \mu - \nu + z_j. \quad (7.3)$$

Figure 7.1 indicates that the interaction is predominantly short range, hence μ and ν must almost cancel in equation (7.3). This is the case for DyVO_4 (Sandercock et al 1972). Taking $\mu = \nu$ and the number of nearest neighbours to be 4

$$j = 2.45 \text{ cm}^{-1}. \quad (7.4)$$

Whether this cancellation of the long range interactions is almost complete can be determined from a measurement of the critical exponent β . The value of β for DyVO_4 and TbVO_4 have recently been determined by Harley and Macfarlane (1975). For DyVO_4 they obtain a value for β of 0.31 which is consistent

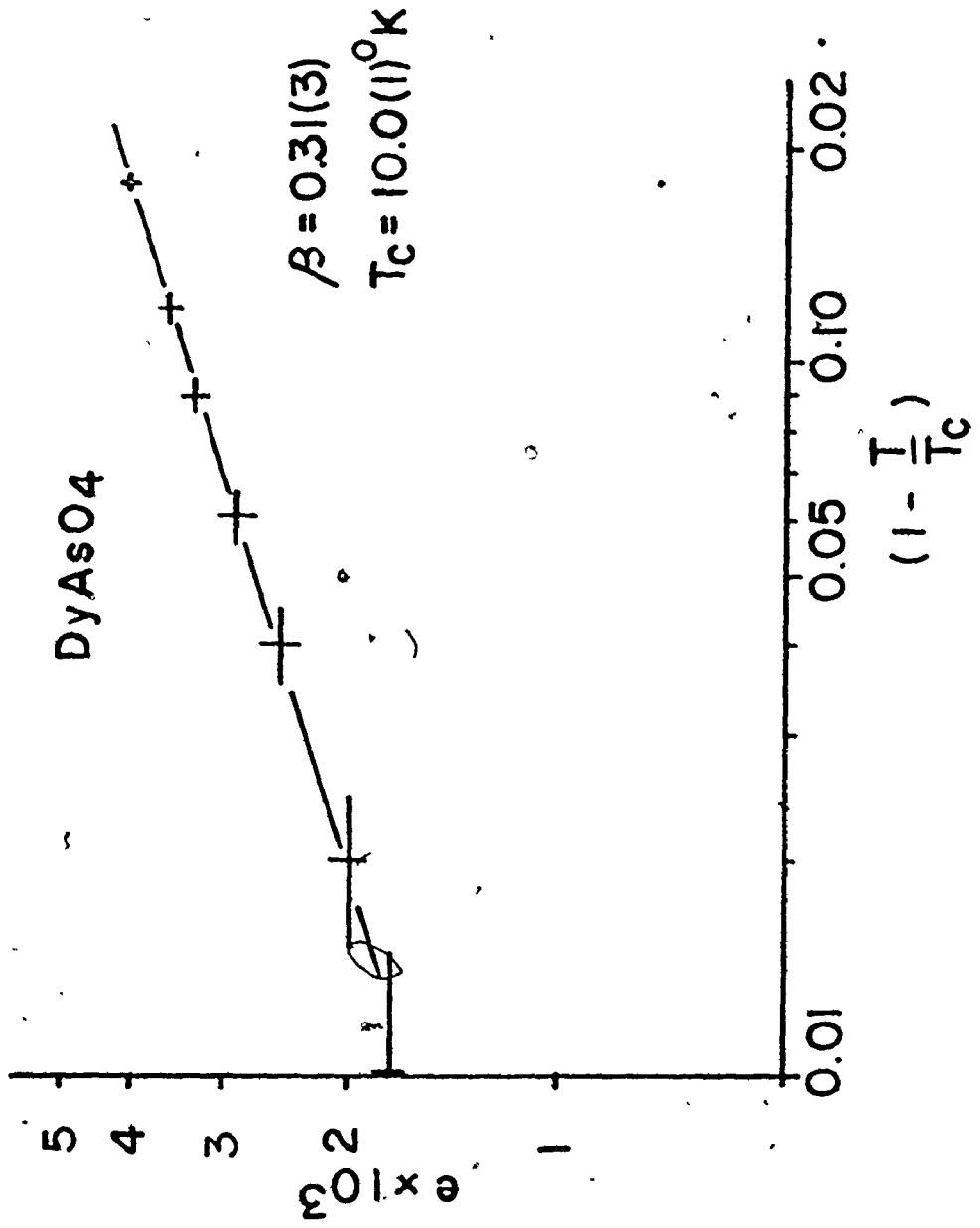
with interactions between nearest neighbours only. It is expected that a similar value would be obtained for DyAsO_4 . For the reason given earlier, data could not be collected arbitrarily close to T_c . However, an attempt has been made to obtain a value of β for DyAsO_4 . The value of T_c and β were obtained by plotting $e^{1/\beta}$ against T for various values of β to get the best linear relationship. Extrapolation to $e=0$ then gives T_D . This procedure gave $\beta = 0.31(3)$ and $T_D = 10.0(1)^\circ\text{K}$. A plot of $\log e$ against $\log(1-T/T_c)$ is shown in Fig. 7.2. Again this is in agreement with very short range interactions. In addition to this dominant short range interaction there are long range couplings to strains and $k=0$ acoustic phonons. The critical behaviour of an Ising system, with a large nearest neighbour interaction and a small long range interaction, has recently been investigated by Amarony (1974). He shows that as T is reduced a cross over from $\beta = 0.3$ to $\beta = 0.5$ (the mean field value) occurs at $(1 - T/T_c)^{7/6} = g$ where g is the ratio of the long range to short range interactions. In this work data was collected down to $(1 - T/T_c) = 0.01$ without any evidence of such a cross over. So an upper bound can be placed on this ratio, that is

$$g < 4.6 \times 10^{-3} \quad (7.5)$$

This means that at least 99.5% of the coupling is short range.

Fig. 7.2

Asymptotic behaviour of the order parameter
yielding the critical exponent β for DyAsO_4 .



Temperature Dependence of the Order Parameter for TbAsO₄

A similar set of experiments was performed on TbAsO₄. These results are shown in Fig. 7.3. The full curve is the result of a mean field calculating using equation (6.31) and equation (6.35). The value of the parameter $\lambda = 19.84 \text{ cm}^{-1}$ was chosen to give the experimental value of $T_c = 28.8^\circ\text{K}$. The coupling parameter η was chosen to give a strain of 1.8×10^{-2} at $T = 10^\circ\text{K}$. The value of the elastic constant $C_{66} = 1.35 \times 10^{11}$ dynes/cm² for TbVO₄ was used in the absence of a value for TbAsO₄. All other parameters used are those given in Table 6.1. The agreement between experiment and the mean field theory is good, indicating that for TbAsO₄ the interaction is predominantly long range. Thus the value of the optic mode coupling coefficient j must be almost zero. The value of the strain coupling coefficient can be obtained in a manner similar to that used for DyAsO₄. This gives

$$\mu = 19.3 \text{ cm}^{-1} \quad (7.6)$$

Comparing this value with λ , it can be seen that the dominant coupling is to the strain, both the optic mode coupling and the acoustic mode coupling being zero.

A value of $\beta = 0.51(5)$ has been obtained for TbAsO₄ in the same manner as for DyAsO₄. Fig. 7.4 shows a plot of $\log(e)$ vs $\log(1-T/T_c)$. This value for β is consistent with the interaction being predominantly long range.

Fig. 7.3

Temperature dependence of the order parameter for TbAsO_4 .

TbAsO₄

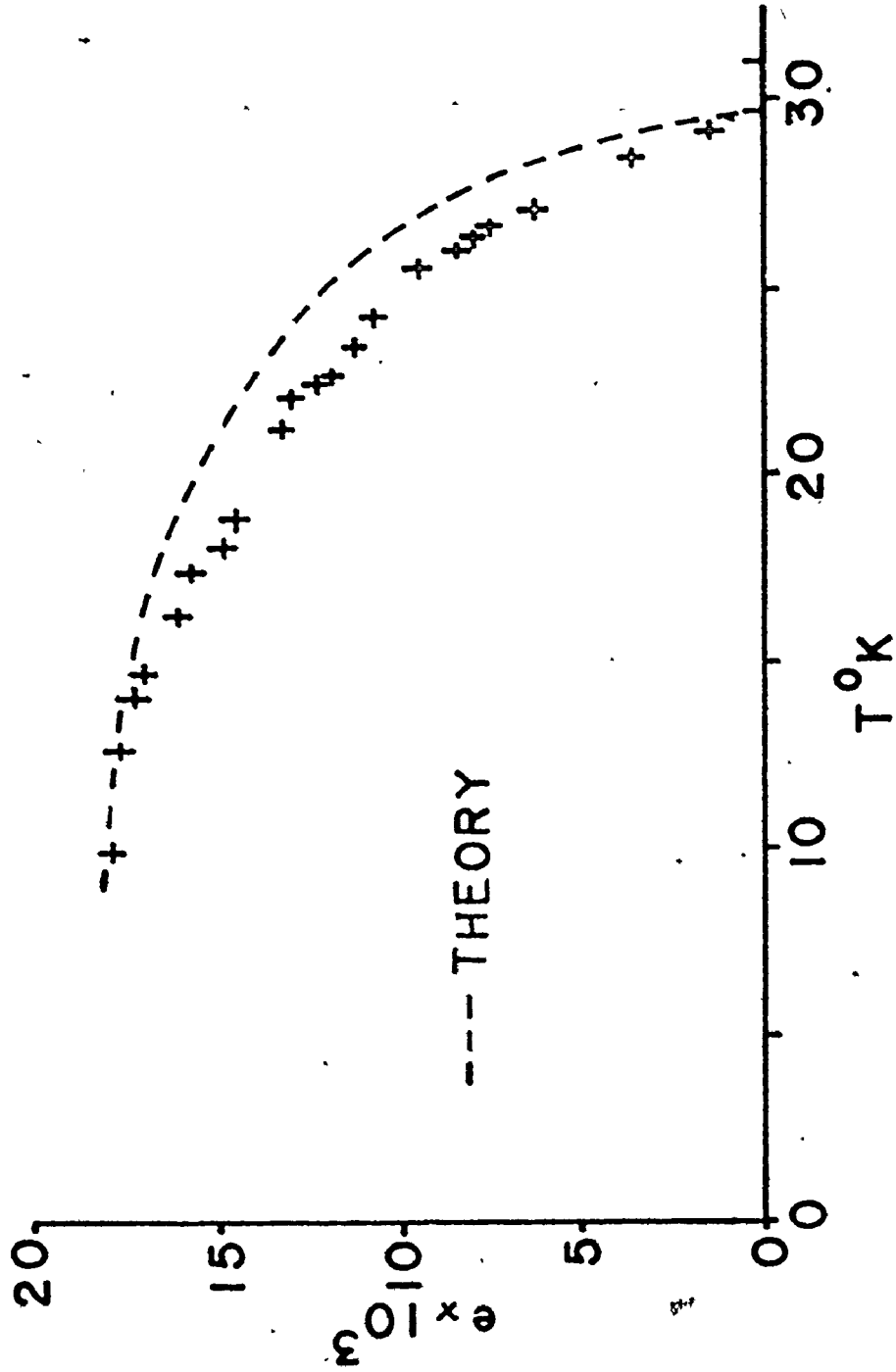
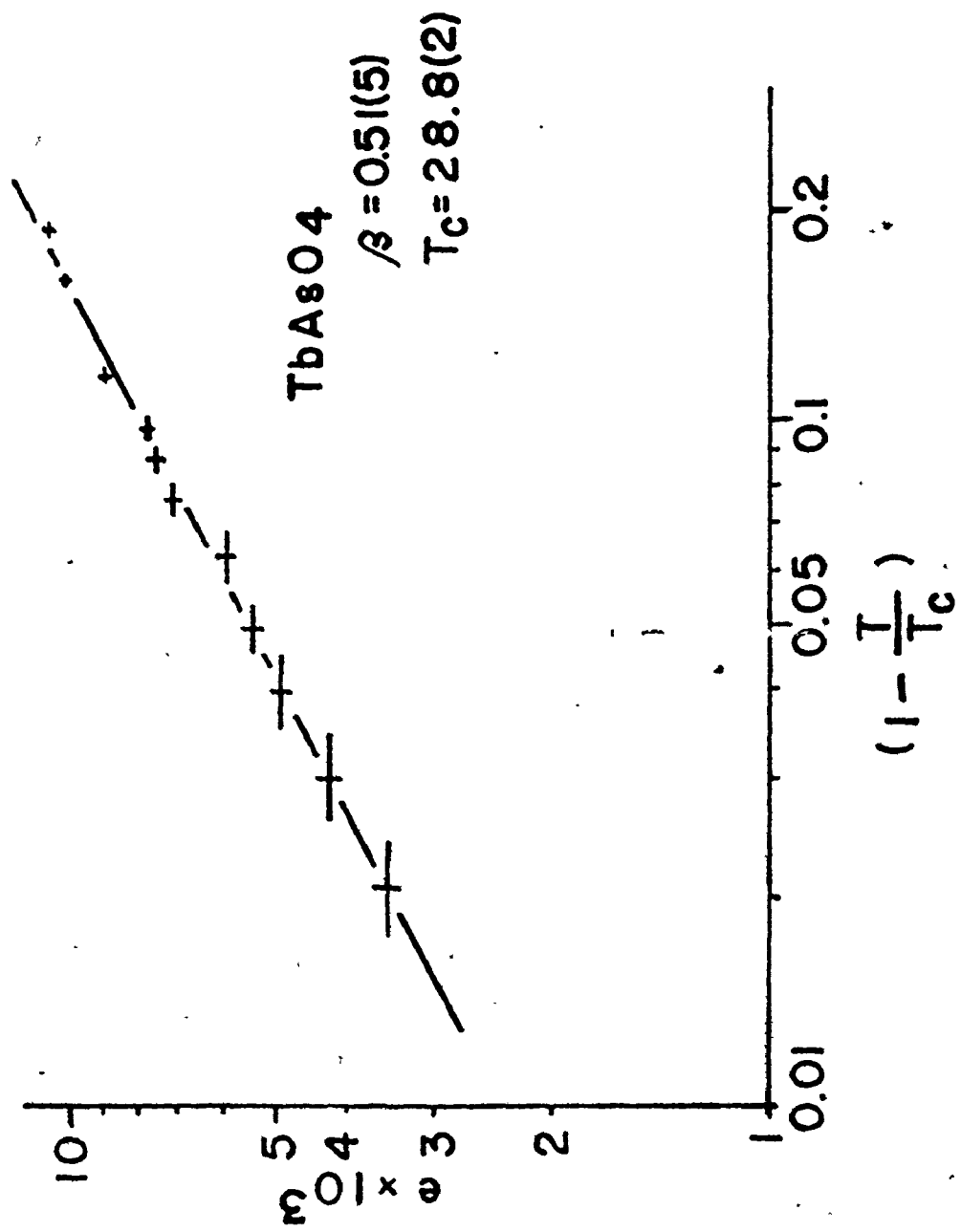


Fig. 7.4

Asymptotic behaviour of the order parameter
yielding the critical exponent β for TbAsO_4 .



Optical Phonon Coupling

In chapter 6 coupling other than to the B_{1g} or B_{2g} mode has been neglected, because Elliot et al. (1972) have shown that the coupling coefficients for other modes are small in comparison with those for the above modes. In particular the coefficients for the A_{1g} modes are smaller by factors of 64 and 32 for $DyAsO_4$ and $TbAsO_4$ respectively. The results presented in Chapter 5 indicate that the coupling to the A_{1g} modes is finite, since local atomic displacements corresponding to these modes are observed. Their contribution to the splitting of the electronic states is proportional to the product of this atomic displacement and the A_{1g} coupling coefficient. In the case of $DyAsO_4$ the displacements in the B_{1g} and A_{1g} modes are of the same order of magnitude, hence the contribution to the A_{1g} is about 2% of that from the B_{1g} mode. The observed value of λ can then be considered as resulting from the B_{1g} coupling only. λ is then related to the phonon coupling coefficient, $S_{B_{1g}}$, by

$$\lambda = S_{B_{1g}} Q_{B_{1g}} / \langle \sigma^3 \rangle = 12.5 \text{ cm}^{-1}. \quad (7.7)$$

Using the value of $Q_{B_{1g}}$ obtained in Chapter 5 for $S_{B_{1g}}$ can be computed using equation (7.7). This gives $S_{B_{1g}} = 706 \text{ cm}^{-1}/\text{\AA}$. For $TbAsO_4$ no evidence of a distortion corresponding to a $k=0$ B_{2g} optic phonon is observed, however a distortion in an A_{1g} mode does occur. The results obtained earlier in this chapter are consistent with almost zero coupling to optic phonons in this case, and so the coupling coefficient for the A_{1g} mode must be very small.

CHAPTER 8

THE COOPERATIVE JAHN-TELLER EFFECT IN THE MIXED CRYSTALS $Tb_x R_{1-x} AsO_4$ (R = Gd, Y or La)

A study of the phase transition in the above mixed systems gives a further test of the applicability of a mean field theory in describing the Jahn-Teller transition in $TbAsO_4$. Within the framework of a molecular field theory the effect of dilution is to replace the parameter λ by λx , where x is the concentration of Jahn-Teller ions. For $TbAsO_4$ the expression for the transition temperature is then given by

$$\frac{\lambda x}{k_B T_c} + \frac{\lambda x}{\epsilon} \sinh\left(\frac{\epsilon}{k_B T_c}\right) = 1 + \cosh\left(\frac{\epsilon}{k_B T_c}\right) . \quad (8.1)$$

A study of the system $Tb_x Gd_{1-x} VO_4$ has recently been conducted by Harley et al. (1974). They find their results are consistent with equation (8.1).

In this work measurements of the temperature dependence of the lattice strain in the mixed systems were made using the technique described in Chapter 7. The variation of the transition temperature with the concentration of Tb^{3+} ions is shown in Fig. 8.1. The solid curve is obtained from equation (8.1) using values of λ and ϵ given in Chapter 7. In the case of the Gd and Y doped crystals there is not

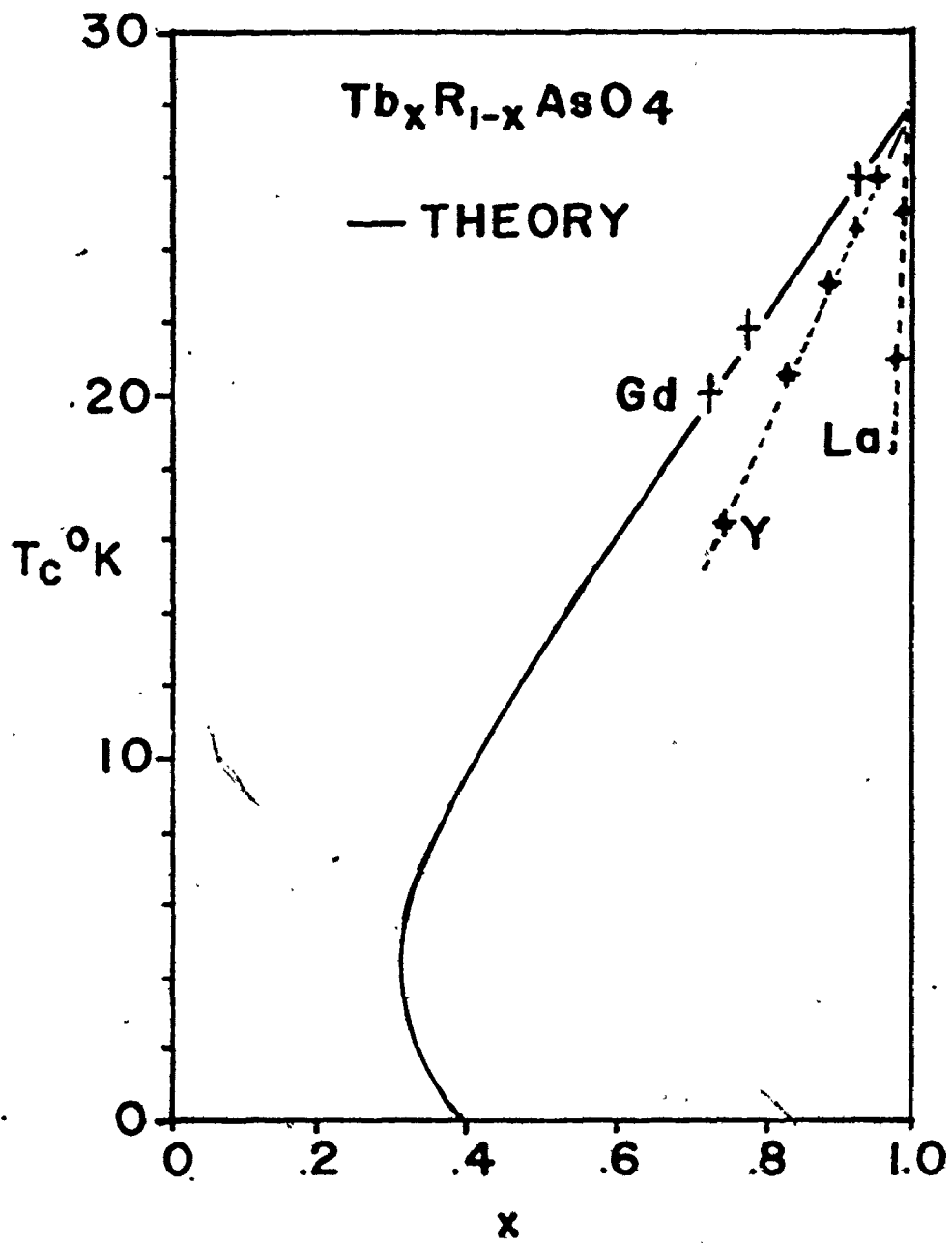
expected to be any interaction which would interfere with the Jahn-Teller coupling between the Tb^{3+} ions (Harley et al. 1974). The results for these crystals are then expected to follow equation (8.1). Clearly this is the case for the Gd doped system but not for $Tb_x Y_{1-x} AsO_4$. It should be noted that Harley et al. also had difficulties when doping $TbVO_4$ with Y. A possible explanation for the departure from theory in this case is the large difference in ionic radius between Tb^{3+} and Y^{3+} . This must result in internal strains in the crystals, which can modify the interaction between the terbium ions. For the two systems considered so far there is isomorphous replacement of the Tb^{3+} ions, since both $GdAsO_4$ and $YAsO_4$ crystallize in the zircon structure. However, this is not the case for $Tb_x La_{1-x} AsO_4$, since $LaAsO_4$ crystallizes in a monoclinic structure (Wyckoff 1965). The departure from theory in this case is possibly due to a combination of strains, resulting from the mismatch in ionic radii and those due to these structural differences..

The temperature dependence of the lattice strain is of the same form for all the mixed systems considered here. This is indicated in Fig. 8.2, which shows the dependence of the reduced strain on the reduced temperature. The fact that this dependence is the same in each case indicates that the interaction is of long range in all the systems, even for the Y and La doped crystals whose behaviour departs from the mean field theory for one reason or another.

It will be noted from Fig. 8.1 that the mean field theory predicts two phase transitions for a range of Jahn-Teller ion concentrations between 0.385 and 0.320. The high temperature transition is from tetragonal to orthorhombic symmetry and the low temperature transition is back to tetragonal symmetry. These transitions occur in a temperature range below that which can be obtained with the low temperature diffractometer, and so the range of concentration studied was not extended into this region. The existence of this interesting double phase transition has been observed in the case of TbVO_4 by Harley et al. (1974).

Fig. 8.1

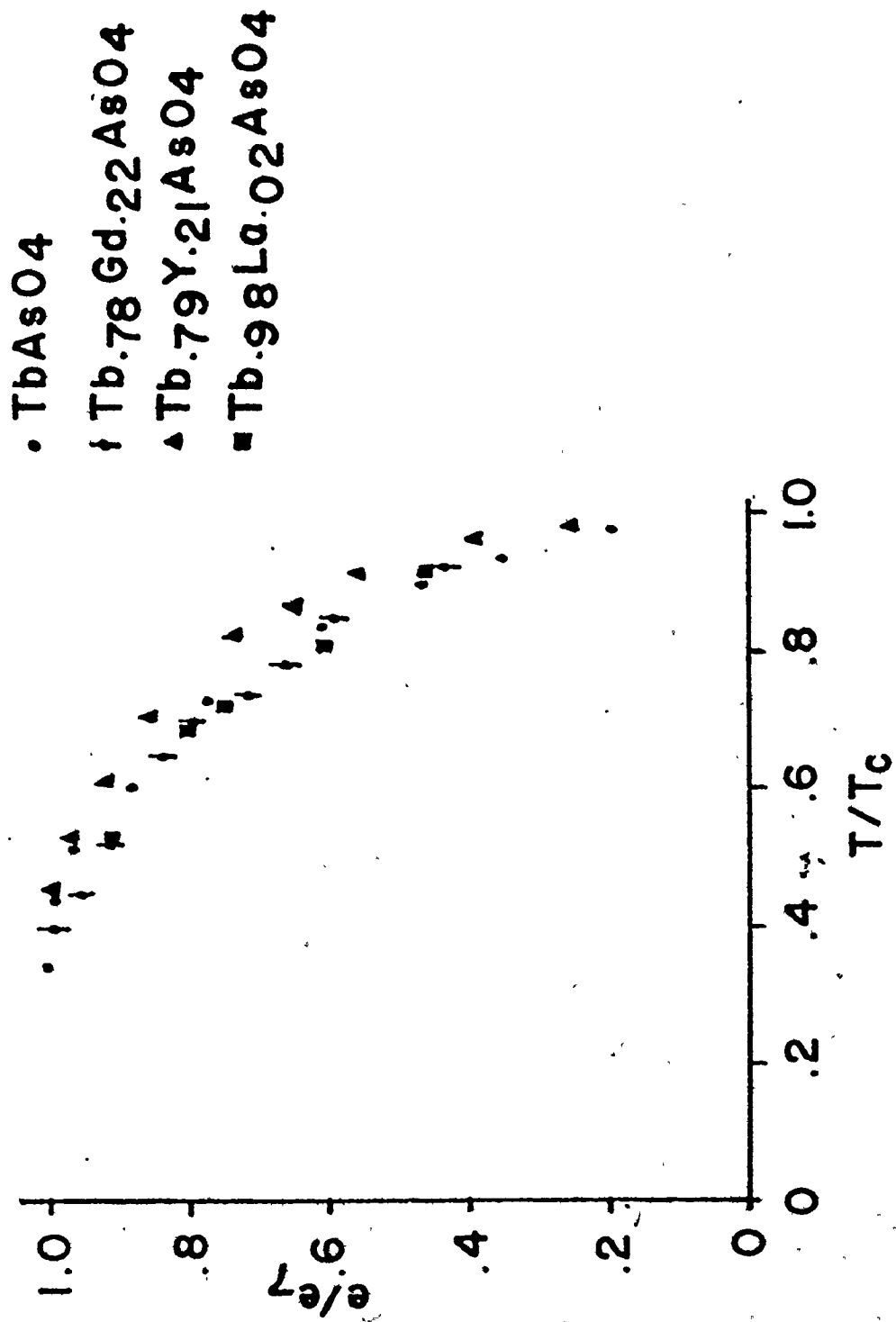
The variation of the transition temperature with composition for the system $Tb_x R_{10-x}AsO_4$ (R = Gd, Y or La).



<

Fig. 8.2

Temperature dependence of the strain for the mixed
crystals $Tb_x R_{1-x} AsO_4$ (R = Gd, Y or La).



CHAPTER 9

CONCLUSIONS

A single crystal diffractometer has been constructed to determine the crystal structure of DyAsO_4 and TbAsO_4 at 6°K. These compounds undergo a second order crystallographic phase transition, at 10°K and 28°K respectively, which is driven by a cooperative Jahn-Teller interaction between the rare earth ions. The low temperature structure of these materials provides information about the nature of the interaction in each case.

The low temperature space groups are both orthorhombic, Imma and Fddd for DyAsO_4 and TbAsO_4 respectively. A comparison of atomic positions in these space groups with those in the high temperature phase, which were determined using a conventional single crystal diffractometer, enables a determination of the symmetry of the phonon modes responsible for the transitions. Furthermore the magnitudes of the shifts in atomic positions between the two phases allows a determination of the coupling strengths to the respective modes.

For DyAsO_4 it was found that coupling to both optic and acoustic phonons is important. The acoustic mode coupling consists of two parts, the strain coupling and coupling to other acoustic phonons whose symmetry is not that of the

distortion of the unit cell. The temperature dependence of the order parameter is consistent with a short range coupling between the Jahn-Teller ions. This indicates that the transition is driven by optic phonons. As the strain coupling is large this means that the two acoustic mode couplings must almost cancel. The optic mode distortions are found to be of symmetry B_{1g} and A_{1g} . The mean field theory predicts that the coupling to the A_{1g} is much smaller than that to the B_{1g} mode, and so on the assumption of only B_{1g} coupling, the relevant coupling coefficient $S_{B_{1g}}$ can be estimated. This is found to be $706 \text{ cm}^{-1}/\text{\AA}$. A measurement of the strain below the transition temperature gives the strain coupling parameter μ , the value is $\mu = 10.4 \text{ cm}^{-1}$. Due to the domination of the optic phonon coupling, the mean field theory does not give an adequate description of the transition in DyAsO_4 . Modifications to this theory which take into account the short range nature of the interaction give a better description.

For TbAsO_4 only the coupling to the strain is important. A distortion corresponding to an A_{1g} optic phonon is observed, but as with DyAsO_4 this gives a minor contribution to the Hamiltonian. This fact is borne out by the temperature dependence of the order parameter, which indicates that the Jahn-Teller coupling is of long range. The strain coupling coefficient in this case is found to be 19.3 cm^{-1} . Because of the long range nature of the interaction the mean field

theory gives a good description of the transition in TbAsO_4 .

A further indication of the applicability of this theory, as applied to the terbium salt, is the variation of the transition temperature with concentration of terbium ions in the system $\text{Tb}_x\text{Gd}_{1-x}\text{AsO}_4$. This variation follows the prediction of the mean field theory.

BIBLIOGRAPHY

- Aharony, A. 1974. Phys. Rev. B8, 3363.
- Baglie, J.A. and Severa, O.J. 1971. J. Solid State Chem. 3, 458.
- Brecher, C., Samelson, H., Riley, R. and Lempicki, A. 1968.
J: Chem. Phys. 49, 3303.
- Cromer, D.T. and Waber, J.T. 1965. Acta Cryst. 18, 104.
- Cruickshank, D.W.J., Pilling, D.E., Bujosa, A., Lovell, E.M.
and Truter, M.R. 1961. Computing Methods and the Phase
Problem in X-ray Crystal Analysis. Edited by R. Pepinsky,
J. M. Robertson and J. C. Speakman (Pergamon Press, New York).
- Dawson, P., Hargreave, M. M. and Wilkinson, G.R. 1971.
J. Phys. C, 4, 240.
- Elliot, R.J., Harley, R.T., Hayes, W. and Smith, S.R.P. 1972.
Proc. R. Soc. A328, 217.
- Ellis, C.J., Gehring, K.A., Leask, M.J.M. and White, R.L. 1971.
J. Physique 32, C1-1024.
- Engleman, R. 1972. The Jahn-Teller Effect in Molecules and
Crystals (Wiley, London).
- Fiegelson, R.S. 1964. J. Am. Ceramic Soc. 47, 257.
- Freeman, A.J. and Watson, R.E. 1965. Magnetism, Vol. IIA.
Edited by G. L. Rado and H. Suhl (Academic Press, New York).
- Fuess, H. and Kallel, A. 1972. J. Solid State Chem. 5, 11.
- Gehring, G.A. and Gehring, K.A. 1975. Rep. Prog. Phys. 38, 1.
- Gehring, G.A., Malozemoff, A.P., Staude, W. and Tyte, R.N.
1972. J. Phys. Chem. Solids 33, 1487.

- Gobel, H. 1972. Phys. Lett. A, 41, 409.
- Gobel, H. and Will, G. 1972. Int. J. Mag. 3, 123.
- Harley, R.T., Hayes, W., Perry, A.M., Smith, S.R.P., Elliot, R.J. and Saville, I.D. 1974. J. Phys. C, 7, 3145.
- Harley, R.T. and MacFarlane, R.M. 1975. J. Phys. C, 8, L451.
- Hutchings, M.T. 1964. Solid State Physics, Vol. 16, Edited by F. Seitz and D. Turnbull (Academic Press, New York).
- Jahn, H.A. and Teller, E. 1937. Proc. R. Soc. A161, 220.
- Kasten, A. and Wüchner, W. 1973. Solid State Commun. 13, 693.
- Kittel, C. 1966. Introduction to Solid State Physics (Wiley, New York).
- Klein, L., Wüchner, W., Kahle, H.G. and Schopper, H.C. 1971. Phys. Stat. Solidi(b) 48, K139.
- Larson, A.C. 1967. Acta Cryst. 23, 664.
- Leask, M.J.M., Maxwell, K.J., Tyte, R.N., Becker, P.J., Kasten, A. and Wüchner, W. 1973. Solid State Commun. 13, 693.
- Lohmüller, Von G., Schmidt, G., Deppish, B., Gremlich, V. and Scherlinger, C. 1973. Acta Cryst. B, 29, 141.
- Sandercock, J.R., Palmer, S.B., Elliot, R.J., Hayes, W., Smith, S.R.P. and Young, A.P. 1972. J. Phys. C, 5, 3126.
- Schafer, W. and Will, G. 1971. J. Phys. C, 4, 3224.
- Shannon, R.D. and Calvo, C. 1973. J. Solid State Chem. 6, 538.

Stout, G.H. and Jensen, L.H. 1968. X-Ray Structure Determination
(MacMillan, New York).

Sturge, M.D. 1967. Solid State Physics, Vol. 20, Edited by F.

Seitz, D. Turnbull and H. Ehrenreich (Academic Press, New York).

Tokanami, M. 1965. Acta Cryst. 19, 486.

Wappler, D. 1974. Phys. Cond. Matter 17, 113.

Will, G. and Schafer, W. 1971. J. Phys. Chem. 4, 811.

Wright, J.C. and Moos, H.W. 1971. Phys. Rev. B, 4, 163.

Wüchner, W., Böhm, W., Kahle, H.G., Kasten, A. and Laugsch, J.

1972. Phys. Stat. Solidi (b) 54, 273.

Wyckoff, R.W.G. 1965. Crystal Structures (Interscience, New York).

Zacharisen, W.H. 1963. Acta Cryst. 16, 1139.